Available online at www.sciencedirect.com
ScienceDirect
ELSEVIER
Icarus 184 (2006) 1–28
ICARUS
www.elsevier.com/locate/icarus

Secular spin dynamics of inner main-belt asteroids

D. Vokrouhlický [*,1], D. Nesvorný, W.F. Bottke

Southwest Research Institute, 1050 Walnut St., Suite 400, Boulder, CO 80302, USA

Received 29 December 2005; revised 6 April 2006

Abstract

Understanding the evolution of asteroid spin states is challenging work, in part because asteroids have a variety of orbits, shapes, spin states, and collisional histories but also because they are strongly influenced by gravitational and non-gravitational (YORP) torques. Using efficient numerical models designed to investigate asteroid orbit and spin dynamics, we study here how several individual asteroids have had their spin states modified over time in response to these torques (i.e., 951 Gaspra, 60 Echo, 32 Pomona, 230 Athamantis, 105 Artemis). These test cases which sample semimajor axis and inclination space in the inner main belt, were chosen as probes into the large parameter space described above. The ultimate goal is to use these data to statistically characterize how all asteroids in the main belt population have reached their present-day spin states. We found that the spin dynamics of prograde-rotating asteroids in the inner main belt is generally less regular than that of the retrograde-rotating ones because of numerous overlapping secular spin–orbit resonances. These resonances strongly affect the spin histories of all bodies, while those of small asteroids ($\lesssim$40 km) are additionally influenced by YORP torques. In most cases, gravitational and non-gravitational torques cause asteroid spin axis orientations to vary widely over short ($\leqslant$1 My) timescales. Our results show that (951) Gaspra has a highly chaotic rotation state induced by an overlap of the s and s_6 spin–orbit resonances. This hinders our ability to investigate its past evolution and infer whether thermal torques have acted on Gaspra's spin axis since its origin.

Keywords: Rotational dynamics; Asteroids, rotation

1. Introduction

Astronomers have long been drawn to study the movement of planetary bodies across the sky. The rotation of these objects, however, did not receive extensive attention until the 1960's–1970's (with the obvious exception of the Earth and Moon), when high-quality data from radio astronomy and spacecraft exploration became available. This has led to numerous insights into how the spin vectors were set during the planet formation epoch (e.g., Lissauer et al., 2000) and how they evolved over Solar System history (e.g., Goldreich and Peale, 1968; Wisdom et al., 1984; Laskar and Robutel, 1993; Néron de Surgy and Laskar, 1997; Correia and Laskar, 2001, 2004). Moreover, recent papers dealing with planets (e.g., Ward and Hamilton, 2004; Hamilton and Ward, 2004) and satellites (e.g., Wisdom, 2004, 2006) show that many interesting results can still be expected in this field.

While there has been abundant theoretical work on planetary and satellite spin dynamics to date, asteroid spin states has been largely neglected. We believe the primary reason for this is that it is difficult to obtain high quality data. This means that most of the detailed modeling work done on specific asteroids has either been associated with spacecraft data (e.g., NEAR at 433 Eros; Souchay et al., 2003; Souchay and Bouquillon, 2005; Vokrouhlický et al., 2005) or has come after years of painstaking observational work (e.g., the "Slivan-state" objects in the Koronis-family; Slivan, 2002; Vokrouhlický et al., 2003). The scientific pioneers who have attempted to make a systematic theoretical analysis of asteroid rotation have mostly come from the Uppsala group (e.g., Skoglöv et al., 1996; Skoglöv, 1997, 1999; Skoglöv and Erikson, 2002). They have focused their attention on the paucity of asteroid spin vectors pointing toward low ecliptic latitudes (e.g., Pravec et al., 2002).

---

[*] Corresponding author. Fax: +420 2 21 91 25 67.
E-mail address: vokrouhl@mbox.cesnet.cz (D. Vokrouhlický).

[1] On leave from Institute of Astronomy, Charles University, V Holešovičkách 2, 18000 Prague 8, Czech Republic.

0019-1035/$ – see front matter © 2006 Elsevier Inc. All rights reserved.
doi:10.1016/j.icarus.2006.04.007

Their work, while interesting and important, was completed before thermal torques were found to play an critical role in the evolution of asteroid spin vectors (e.g., Rubincam, 2000; Bottke et al., 2002a). These torques have been shown to radically change the rotation rates and obliquities of diameter $D \lesssim 40$ km asteroids in the main belt. Together with several advances in numerical methods, we can now investigate the long-term evolution of asteroid spin states in greater detail than was previously possible.

In this paper, we analyze how spin–orbit secular resonances and thermal torques (for $D \lesssim 40$ km objects) affect the evolution of asteroid spin vectors in the inner main belt, the zone where asteroids are most easily observed. We avoid the "infiniteness-of-cases trap" by selecting a limited number of specific asteroids here (e.g., 951 Gaspra). Using these bodies, we investigated how particular parameter dependencies affect spin vector evolution and explored several examples of possible asteroid spin evolution for representative asteroids across the inner main belt.

We believe our work is timely because spin rate and orientation data for both near-Earth and the main-belt asteroids have increased significantly over the past decade. There are currently more than 120 main-belt asteroids with known rotation states determined using various techniques as opposed to about 80 in 2002. In the coming years this trend will likely accelerate, especially if the data from astrometric surveys (e.g., Pan-STARRS) and/or the GAIA space project can be used to derive this information (e.g., Kaasalainen, 2004). Ideally, this data will alllow us to examine the evolution of spin vectors in a statistical sense, which in turn will yield a better understanding of secular spin dynamics in the main asteroid belt.

While the results of these future observation programs are unknown, we can use the existing asteroid-rotation data to probe several interesting unsolved problems (see also Pravec et al., 2002). For instance, it is well established that the distribution of rotation rates of main-belt asteroids changes from a near Maxwellian for large ($D \geqslant 40$ km) objects to more irregular distribution for small ($D \leqslant 40$ km) objects. In particular, the small body rotation distribution is characterized by an excess of both fast and slow rotating asteroids. Some researchers have attempted to empirically fit the rotation rate distribution of small asteroids (e.g., Fulchignoni et al., 1995; Donnison and Wiper, 1999) and relate them to samples of bodies with different spectral taxonomy. The existing data, however, is ambiguous on whether taxonomic type plays a strong role in asteroid spins. We argue that as of yet, no model of rotation rate evolution is fully consistent with the distribution of rotation rates of small objects. Of particular interest is the origin of the anomalously slowly-rotating asteroids with spin periods lasting, in some cases, days or weeks.

There are also several on-going mysteries involving related to the distribution of asteroid spin poles (see discussion in Pravec et al., 2002). For example, since the 1980s researchers have suspected that the pole distribution might be skewed toward ecliptic poles, with significantly fewer asteroid rotation axes residing in the ecliptic plane. The newest data compilations (e.g., Skoglöv and Erikson, 2002) still appear to support this conclusion. This irregular behavior seems to affect both large and small asteroids, while considerably less information is known about poles of $D \leqslant 40$ km main-belt asteroids. La Spina et al. (2004) suggested that the ecliptic-pole deficiency still exists for near-Earth asteroids (NEAs). While several hypotheses have been suggested to solve this problem, none, in our opinion, are yet completely satisfying.

A second example is the surprising abundance of retrograde-rotating NEAs; they are twice as numerous as the prograde-rotating ones (La Spina et al., 2004). Models that track the delivery of asteroids from the main belt to the NEA region (e.g., Bottke et al., 2002b; Morbidelli and Vokrouhlický, 2003) suggest this difference may be a byproduct of both Yarkovsky drift and resonant dynamics in the main belt. In particular, the powerful ν_6 secular resonance at the innermost border of the main belt, which provides nearly 40% of all NEAs (Bottke et al., 2002b), can only be approached by main-belt asteroids drifting inward. According to Yarkovsky thermal drift models, this means the objects entering into the ν_6 need to have must have retrograde spins. Despite the success of this hypothesis, however, theorists have yet to study in detail how spin pole distributions evolve during NEA delivery from the main belt to the planet-crossing region (for an example see Vokrouhlický et al., 2005).

Another motivation for investigating the spin vector evolution of small main-belt asteroids comes from an analysis of the asteroid families' structures in proper element space. Vokrouhlický et al. (2006a, 2006b, 2006c) showed that small family members are frequently the most distant from each family's center in terms of semimajor axis. This may be because thermal YORP torques cause their rotation poles to slowly align with their ecliptic poles and hence increase their Yarkovsky drift rates (see also Rubincam, 2000; Vokrouhlický et al., 2003). By carefully comparing model results with observations in several families, they found it might be possible to use this information like a clock to determine the time elapsed since the family's formation. These models of pole evolution, however, contain several rather crude approximations and do not include all of the relevant torques that can affect asteroid evolution. We have tried to rectify some of these issues in this paper (Section 5). When we are satisfied we have a reasonable model of how these torques feedback into our asteroid spin vector and Yarkovsky drift evolution computations, we will then be able to return our family age estimates and revise them accordingly.

2. Secular spin–orbit dynamics: Basic formulation

We first briefly review the rigid-body spin dynamics formalism needed for our work. We restrict our work here to the case of principal-axis rotation; this means that free motion (tumbling) of the spin axis in the body-frame is not allowed. Only a limited number of asteroids with large-amplitude tumbling spin axes are known today (e.g., Pravec et al., 2005). We also will not be modeling short-period effects or small-amplitude details of asteroid rotation (see Souchay et al., 2003; Souchay and Bouquillon, 2005). Instead, we focus here on characterizing the evolution of the spin axis over long timescales (comparable to or longer than the asteroid's orbital period about the Sun). The asteroid's orbital motion is assumed to be decoupled from the spin axis evolution, but it can be affected by gravitational perturbations from the planets.

We denote the rotational angular momentum vector by $\mathbf{L}$. The Euler equation, central to our problem, can then be defined as (e.g., Colombo, 1966; Holland and Sperling, 1969):

$$\frac{\mathrm{d}\mathbf{L}}{\mathrm{d}t} = -\left[\alpha(\mathbf{n}\cdot\mathbf{e})\mathbf{n} + \boldsymbol{\sigma}\right] \times \mathbf{L} + \mathbf{T}_{\mathrm{NG}}. \tag{1}$$

The right side of (1) contains two explicit contributions. The first term in the bracket is the orbit-averaged gravitational torque due to the Sun (e.g., Bertotti et al., 2003). It depends on the direction of the spin axis (unit vector $\mathbf{e}$) with respect to the normal $\mathbf{n}$ to the instantaneous (osculating) orbital plane. Dependence on the rotation rate, ω, appears through the factor:

$$\alpha = \frac{3}{2}\frac{n^2}{\omega}\frac{\Delta}{\eta^3}, \tag{2}$$

which determines also precession frequency at zero obliquity. Here n is the mean orbital motion, $\eta = \sqrt{1-e^2}$, with e the orbital eccentricity, and

$$\Delta = \frac{C - \frac{1}{2}(A+B)}{C}. \tag{3}$$

This last equation characterizes the dynamical flattening of the body ($A \leqslant B \leqslant C$ are the principal values of the inertia tensor).

The value of α is fundamental for understanding the spin dynamics of an asteroid. We have $\alpha \simeq 1330.6\xi/(a\eta)^3$ arcsec/yr, where the semimajor axis a is given in AU and $\xi = \Delta(P/6\ \mathrm{h})$, with $P = 2\pi/\omega$ is the rotation period in hours (since $e \lesssim 0.15$ in most cases one can also put $\eta \simeq 1$). Since 6 h is a characteristic rotation period for most asteroids, we introduce a scaled variable $P_6 = P/6$ h of the order of unity. The parameter Δ ranges from 0 for near-spherical bodies to 0.5 for highly-elongated objects. Most $D \lesssim 40$ km asteroids are thought to have values in the 0.2–0.4 range (e.g., Vokrouhlický and Čapek, 2002, their Fig. 2). Observational lightcurve data can usually be used to determine P to reasonable accuracy. Determining the asteroid's spin vector $\mathbf{e}$ from this data, however, is more challenging unless observations were taken at several different times during the asteroid's revolution around the Sun. Still, the main uncertainty in computing α for a given body usually stems from a badly constrained value of Δ.

The second term in the bracket of Eq. (1)—$\mathbf{L} \times \boldsymbol{\sigma}$—is due to the fact that the quantities in this equation have been defined in a moving reference frame. The vector $\boldsymbol{\sigma}$ characterizes the motion of the reference frame with respect to an inertial system. Traditionally, one chooses the asteroid's osculating orbit plane to be the reference frame. That has the advantage of turning the normal vector $\mathbf{n} = (0,0,1)^T$ and $\boldsymbol{\sigma}$ into simple expressions. The latter expression depends on the orbit plane's evolution in space (i.e., changes to the longitude of node Ω and inclination I). As described by Breiter et al. (2005) as well as many others, it is convenient to define the x-axis as a line in the orbital frame rotated by $-\Omega$ from the nodal line. That convention removes any problem that might occur for small inclinations and yields $\boldsymbol{\sigma} = (\mathcal{A}, \mathcal{B}, -2\mathcal{C})^T$ with (see also Laskar and Robutel, 1993; Néron de Surgy and Laskar, 1997):

$$\mathcal{A} = \dot{I}\,\cos\Omega - \dot{\Omega}\sin I \sin\Omega, \tag{4}$$

$$\mathcal{B} = \dot{I}\,\sin\Omega + \dot{\Omega}\sin I \cos\Omega, \tag{5}$$

$$\mathcal{C} = \dot{\Omega}\sin^2 I/2. \tag{6}$$

Note that the over-dot means a time derivative of the variable.

The last term in (1)—$\mathbf{T}_{\mathrm{NG}}$—describes all perturbing torques of non-gravitational origin. Neglecting internal dissipation effects for this study, the most important long-term torque is caused by reflected and thermally re-radiated sunlight, or what is commonly now called the Yarkovsky–O'Keefe–Radzievskii–Paddack (YORP) effect (e.g., Rubincam, 2000; Vokrouhlický and Čapek, 2002; Čapek and Vokrouhlický, 2004).

Like many other problems in mathematical physics, analytical and numerical approaches often profit when different formulations are used. The minimum-parameter approach—suitable in analytical methods—would first split $\mathbf{L}$ into components of angular frequency of rotation ω and $\mathbf{e}$. This would allow us to write $\mathbf{L} = C\omega\mathbf{e}$, with the unitary vector $\mathbf{e}$ defined in the second step using two angular parameters: $\mathbf{e} = (\sin\epsilon\sin\psi, \sin\epsilon\cos\psi, \cos\epsilon)^T$. Recall that the x-axis has been rotated by $-\Omega$ with respect to the usual orbital frame with origin at the nodal line. Here ϵ is the obliquity and ψ is the precession angle (note $\mathrm{d}\psi/\mathrm{d}t > 0$ means retrograde precession). When $\mathbf{T}_{\mathrm{NG}} = 0$, or when it is analyzed from a perturbation theory perspective, the problem is reduced to a 1-D Hamiltonian:

$$\mathcal{H}(X,\psi;t) = \frac{\alpha}{2}X^2 - 2\mathcal{C}X + \sqrt{1-X^2}(\mathcal{A}\sin\psi + \mathcal{B}\cos\psi), \tag{7}$$

where the momentum is defined as $X = \cos\epsilon$.

A useful approximation occurs when $\mathcal{A}$, $\mathcal{B}$ and $\mathcal{C}$ are represented using a finite Fourier series such as[2]

$$\mathcal{A} = \sum_j A_j \sin\left(s_j t + \phi_j^A\right), \tag{8}$$

$$\mathcal{B} = \sum_j B_j \cos\left(s_j t + \phi_j^B\right), \tag{9}$$

$$\mathcal{C} = \sum_j C_j \cos\left(s_j t + \phi_j^C\right). \tag{10}$$

Note that the problem is still challenging to deal with because the equations of motion are both non-linear and contain time-dependent forcing terms. It reduces to an integrable case only when the $\mathcal{A}$, $\mathcal{B}$ and $\mathcal{C}$ spectrum contains just a single line with a frequency s (i.e., when the orbital plane maintains a constant inclination to the reference frame and precesses uniformly in space with the frequency s). This problem has been thoroughly studied and is generally known as a Colombo top (e.g., Colombo, 1966; Henrard and Murigande, 1987). We will not repeat its many known properties here except for those relevant to our study.

---

[2] We note that the Fourier spectrum of $\mathcal{A}$, $\mathcal{B}$ and $\mathcal{C}$ at low inclinations closely matches that of the inclination complex vector $\sin I/2\exp(\imath\Omega)$.

The Colombo top is a two-parameter problem, with the first parameter being the inclination I of the precessing orbital plane and the second being $\kappa = \alpha/(2s)$. Given particular values of these two parameters, the phase space can contain 2–4 equilibrium points (i.e., fixed positions of the spin axis with respect to the moving orbital plane). For a chosen value of I, the bifurcation from 2 to 4 points occurs for (e.g., Henrard and Murigande, 1987)

$$\kappa_\star = -\frac{1}{2}\left(\sin^{2/3} I + \cos^{2/3} I\right)^{3/2} \tag{11}$$

which ranges from -0.5 (for $I = 0°$ and $90°$) to -1 (for $I = 45°$). In the more interesting case of 4 equilibria, when $\kappa < \kappa_\star$, one of them—the Cassini state 4—becomes an unstable locus of homoclinic orbits that surround a resonance zone about a stable equilibrium—the Cassini state 2. The resonance is then characterized by the libration of a critical angle $\phi \sim -\psi - st$. Since the dynamics here concerns the commensurability of the asteroid's orbital plane and its spin axis precession frequencies s and $-\dot{\psi}$, this introduces the possibility of secular spin–orbit resonances. Understanding such resonances is essential to computing the long-term spin dynamics of asteroids with prograde rotation states.

Secular spin–orbit resonances tend to complicate the evolution of asteroid spin vectors across the main belt (and especially in its inner zone) because at least *two frequencies* contribute, and usually dominate, the spectrum in (8)–(10): (i) the proper frequency s, and (ii) the forced frequency $s_6 \simeq -26.34$ arcsec/yr. The value of s depends on proper orbital elements and ranges from $\simeq -35$ arcsec/yr in the inner belt to $\simeq -75$ arcsec/yr in the outer belt[3] (Fig. 1). In spite of other (weaker) frequencies contributing, we find it useful to introduce this two-frequencies model as an approximate tool. The main advantage is that the problem reduces the to a 2-D Hamiltonian flow. A classical chaotic-zone-tracer technique of surfaces-of-section (e.g., Morbidelli, 2002) can then be used to explore the properties of an asteroid's spin axis evolution. We take advantage of this approach in Section 3 to determine the fundamental properties of long-term spin dynamics for selected asteroids.

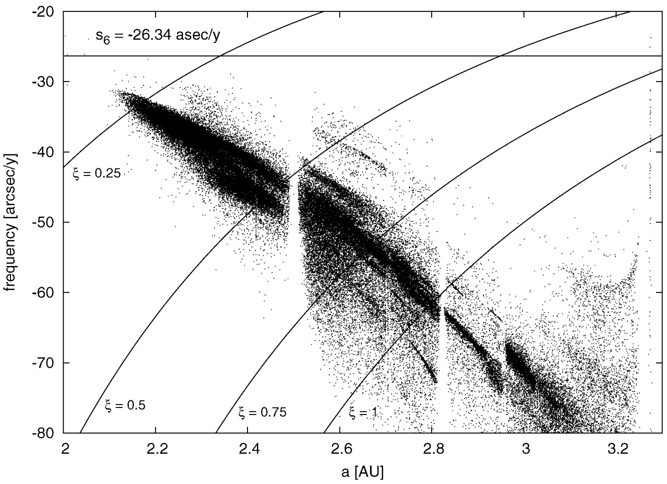

Fig. 1. Proper frequency s of the nodal drift (dots) for nearly 100,000 main-belt asteroids (source: `AstDyS` as of July 2005). The mean value of s approximately increases as $s \sim a^{5/2}$; the large scatter at each a is due to eccentricity and inclination dependence. Solid lines indicate the value of $-\alpha$ for different values of the parameter $\xi = \Delta(P/6\,\mathrm{h})$ (where P is rotation period in hours; Δ is the dynamical flattening) and assuming mean eccentricity $e \sim 0.1$.

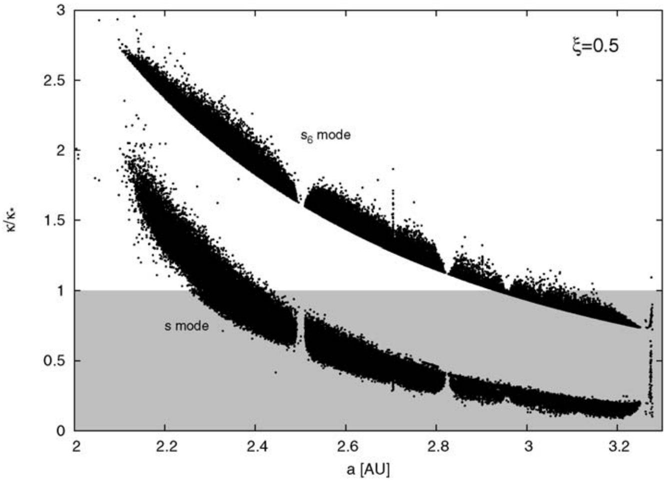

Fig. 2. The ordinate shows ratio $\kappa/\kappa_\star$ (see the text) probing existence both of the s frequency (bottom symbols) and s_6 frequency (upper symbols) spin–orbit resonance for nearly 100,000 main-belt asteroids. A value larger than unity implies the resonance exists (conversely, the resonance does not exist when $\kappa/\kappa_\star < 1$; shaded zone). For definiteness, we chose a particular value of $\xi = \Delta P_6 = 0.5$, but the ratio $\kappa/\kappa_\star$ scales as $\propto \xi$ for different values of this parameter. While the s_6 resonance exists basically across the whole main asteroid belt region, the typically stronger s resonance occurs merely in its inner zone. Simultaneous existence of the close-by s and s_6 resonances is expected to trigger irregular behavior of asteroid spin parameters for prograde-rotating bodies.

Fig. 2 shows the ratio $\kappa/\kappa_\star$ for a large number of main-belt asteroids and for the secular spin–orbit resonances associated with the s- and s_6-modes. The proper elements and frequency s were taken from the `AstDyS` database (http://newton.dm.unipi.it/). We assumed an arbitrary value of $\xi = \Delta P_6 = 0.5$.[4] As mentioned above, the resonance exists when $\kappa/\kappa_\star > 1$ (note κ is negative). Fig. 2 indicates the s_6 spin–orbit resonance is present throughout the entire asteroid belt. Its importance, however, is restricted because of the small forced inclination values ($\lesssim 1.5°$). Still, this resonance can produce spectacular phenomena such as the near-parallel orientation of several Koronis members (i.e., those in Slivan states; Vokrouhlický et al., 2003). On the other hand, the powerful s spin–orbit resonance can affect asteroids with large proper inclination values ($\sim 5°$–$10°$; Fig. 3). Under normal conditions, however, it only exists in the inner main belt. For this reason, we pay particular attention to this zone in our numerical runs below, with the interaction between the s and s_6 spin–orbit resonances producing many curious effects. Note that in Appendix A, we derive a simple resonance overlap criterion in order to characterize the importance of this interaction.

To explore asteroid spin dynamics numerically, it is more useful to examine the evolution of ω and $\mathbf{e}$ directly (e.g., Breiter

---

[3] For Trojan group of asteroids, librating about the Lagrangian points of Jupiter, the s frequency is typically small.

[4] Because $\alpha \propto \xi$, we note that the results in Fig. 2 scale as $\propto \xi$.

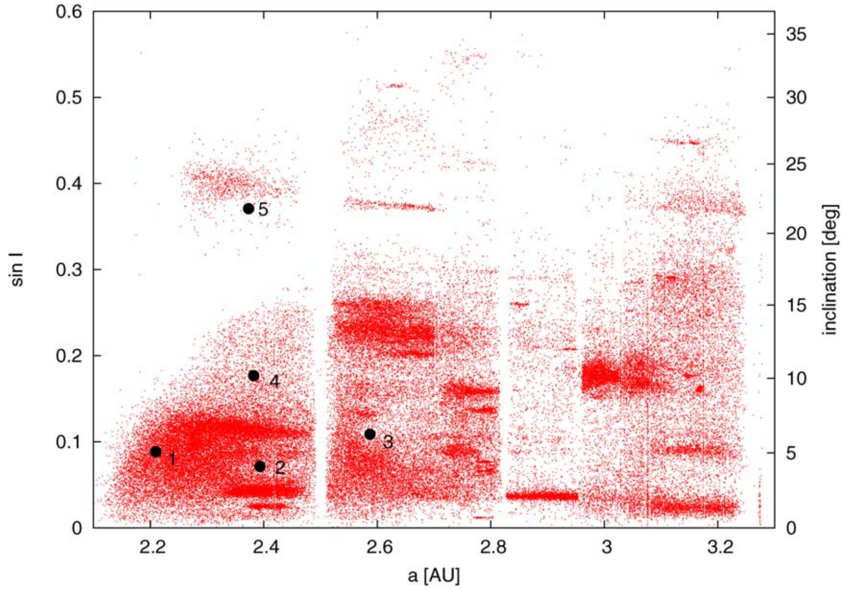

Fig. 3. Synthetic proper elements of nearly 100,000 main-belt asteroids from the `AstDyS` database projected onto the semimajor axis a vs sine of inclination $\sin I$ plane. Symbols highlight asteroids whose spin axis evolution is studied in this paper: (i) 1—(951) Gaspra (very similar to (8) Flora), (ii) 2—(60) Echo, (iii) 3—(32) Pomona, (iv) 4—(230) Athamantis, and (v) 5—(105) Artemis. They sample different values of the heliocentric distance and different inclination values, both relevant for the spin axis behavior.

et al., 2005). We have done this by rewriting Eq. (1) as

$$\frac{\mathrm{d}\mathbf{e}}{\mathrm{d}t} = \mathbf{e} \times \left[\frac{\partial \mathcal{H}}{\partial \mathbf{e}} + \boldsymbol{\tau}^\star\right], \tag{12}$$

$$\frac{\mathrm{d}\omega}{\mathrm{d}t} = \omega\, \mathbf{e} \cdot \boldsymbol{\tau}, \tag{13}$$

where $\mathbf{T}_{\mathrm{NG}}$ is represented by two orthogonal components: $\boldsymbol{\tau} = \mathbf{T}_{\mathrm{NG}}/(C\omega)$ and $\boldsymbol{\tau}^\star = \boldsymbol{\tau} \times \mathbf{e}$. The Hamiltonian $\mathcal{H}$, now rewritten using the new variables, is

$$\mathcal{H} = \frac{\alpha}{2} e_3^2 + \boldsymbol{\sigma} \cdot \mathbf{e}. \tag{14}$$

The Hamiltonian-only part meets the conditions needed to allow us to use an efficient Lie–Poisson integrator set (Breiter et al., 2005), while the remaining part, which depends on $\boldsymbol{\tau}$ and $\boldsymbol{\tau}^\star$, may be treated using the perturbation equations if small.

In this paper, we solve the Hamiltonian part of the equation using the two-component splitting (LP2) method of the Lie–Poisson integrator (Breiter et al., 2005). This formalism yields computational speeds that are 1–2 orders of magnitude higher than general-purpose integrators. An additional advantage of LP2 splitting is that we avoid calculating $\boldsymbol{\sigma}$; instead, we only need the time series of the orbital elements Ω and I. Those are obtained by direct numerical integration of the asteroid orbit using `swift` code (e.g., Levison and Duncan, 1994) with all relevant planetary perturbations taken into account. The application of YORP torques $\mathbf{T}_{\mathrm{NG}}$ are simplified by (i) only using orbit-averaged values and (ii) dropping the YORP contribution to the precession rate. The relevant equations then become (see also Rubincam, 2000; Vokrouhlický and Čapek, 2002; Čapek and Vokrouhlický, 2004)

$$\frac{\mathrm{d}\omega}{\mathrm{d}t} = f(e_3), \tag{15}$$

$$\frac{\mathrm{d}e_3}{\mathrm{d}t} = \frac{g(e_3)}{\omega} \tag{16}$$

(e_1 and e_2 are constants), where $f(x)$ and $g(x)$ are functions that are numerically precomputed for a given asteroid. With this, the formal solution of (15) and (16) becomes:

$$\omega = \omega_0 \Psi(e_3; e_{3,0}), \tag{17}$$

$$\frac{t - t_0}{\omega_0} = \int_{e_{3,0}}^{e_3} \mathrm{d}x\, g(x) \Psi^{-1}(x; e_{3,0}), \tag{18}$$

with

$$\Psi(x; e_{3,0}) = e^{\int_{e_{3,0}}^{x} \mathrm{d}y\, f(y)/g(y)}. \tag{19}$$

Although this method neatly circumvents the problems that would arise for solutions near $\omega \simeq 0$ and $|e_3| \simeq 1$, its practical use is undermined by its complicated algebraic structure and an implicit solution of $e_3(t - t_0; e_{3,0})$ in (18). For this reason, we use here the simplest possible, Euler-type solution of (15) and (16).

3. Examples of spin dynamics the inner-belt: No YORP included

We consider here a number of inner and central main-belt asteroids as sample test cases for how bodies in these regions might undergo spin axis evolution. Fig. 3 shows their location projected in proper semimajor axis a vs. proper inclination I. We have chosen 3 asteroids that follow a progression toward larger a while keeping roughly the same I: (951) Gaspra → (60) Echo → (32) Pomona. Two more were chosen because they have the same a as (60) Echo but different I values: (60) Echo → (230) Athamantis → (105) Artemis. These cases were also chosen because we have some information about their rotation rate and spin axis orientation. Our main source for this data is the catalog compiled at the Poznań Observatory under the auspices of A. Kryszczyńska (http://www.astro.amu.edu.pl/). Their work builds on an earlier effort of P. Magnusson (http://www.psi.edu/pds/). Additional data, when needed, is obtained from the literature.

Sections 3 and 4 contain our analysis of these objects, which was taken in two steps. For the first step, we only included gravitational torques and set $\mathbf{T}_{\rm NG} = 0$ in Eq. (1) (Section 3). This choice allowed us to study how various parameters and interacting secular spin–orbit resonances would affect the evolution of asteroid spin vectors without the added complication of YORP torques. Note that these results are especially relevant for $D \gtrsim 50$ km asteroids that are minimally affected by YORP torques. We selected asteroids in our sample with obliquity values $\epsilon < 90°$ because only those bodies with prograde spins are affected by spin–orbit resonances. The long-term spin dynamics of retrograde-rotating objects is mostly influenced by regular precession; we do not consider those effects in this paper. For the second step, we added thermal torques into our analysis (Section 4), which significantly increases the complexity of evolutionary scenarios for asteroid spins.

3.1. (951) Gaspra

(951) Gaspra, a member of the Flora family with osculating orbital elements of semimajor axis $a = 2.21$ AU, eccentricity $e = 0.174$, and inclination $I = 4.10°$, was visited by the Galileo spacecraft during its short flyby in October 1991. As a result, we have high-quality data on its shape and rotation. Here we use the rotation rate and pole determination made by Davies et al. (1994), who give $P = 7.04$ h, $\ell = 19°$ and $b = 21°$ for the ecliptic longitude and latitude of the pole. Their pole parameters have a one degree standard deviation, small in comparison to estimates of asteroid spin vectors determined by ground-based data. Galileo imaging also provided us with an approximate shape of the asteroid (e.g., Thomas et al., 1994). Here we use the $2° \times 2°$ shape model found in http://www.psi.edu/pds/, that we converted into a 5040-hedron with triangular facets for our YORP modeling. Assuming Gaspra has a homogeneous density distribution, we estimate that $\Delta = 0.305$ with a $\sim$1% uncertainty. Gaspra's cratering record suggests it is relatively young, $\sim$200–500 My (e.g., Greenberg et al., 1994; Chapman, 2002). The upper limit on Gaspra's age is set by the age of the Flora family, which ranges from 0.5–1.0 Gy (Nesvorný et al., 2002). Note that Gaspra's mean collisional lifetime is likely longer than a Gy (Bottke et al., 2005). Thus, at present we cannot say whether Gaspra's surface has recorded cratering events since the formation of the Flora family or whether it has been subject to one or more powerful crater erasure events since that time.

The orbit of Gaspra, as well as all other asteroids considered in this paper, was taken from the `AstOrb` database (Bowell et al., 1994). We propagated Gaspra's current orbit forward 50 My and backward 1 My to get a reasonable characterization of its orbital evolution (the initial time was Jan 1.0, 2000). The same technique was used by Vokrouhlický et al. (2005) to analyze different modes in the Fourier representation of the orbital plane precession in space. Namely, the complex inclination vector $\sin I/2 \exp(\imath\Omega)$ is passed piecewise through a Fourier filter using a running window of 1 My width. The proper mode with frequency $s \simeq -35.93$ arcsec/yr and amplitude of $I \simeq 4.88°$ was found to dominate, with its initial phase $\simeq 274.8°$, close to the osculating longitude of the node. The second most important term was that of the forced s_6 frequency, with $I \simeq 1.16°$ and an initial phase of $\simeq 309.8°$. These data, together with similar information about the other asteroids considered in this paper, are summarized in Table 1. Because Gaspra is located in the inside part of the inner part, a number of other Fourier terms also affect the local representation of $\sin I/2 \exp(\imath\Omega)$, which limits the usefulness of the two frequency model. Nevertheless, we find our analysis allows us to glean several interesting insights into the long-term dynamics of Gaspra's spin vector.

Table 1
Sample of asteroids considered in this paper and orbital parameters relevant for their long-term spin dynamics[a]

Asteroid	a (AU)	s (arcsec/yr)	$I_{\rm p}$ (°)	$\Omega_{\rm p}$ (°)	I_6 (°)	Ω_6 (°)
32 Pomona	2.587	−50.63	6.10	228	0.68	307
60 Echo	2.393	−46.58	4.09	205	0.74	307
105 Artemis	2.373	−37.57	21.56	167	1.77[b]	240
230 Athamantis	2.382	−38.12	10.17	242	1.10	307
951 Gaspra	2.210	−35.93	4.88	275	1.16	310

[a] Listed are: proper semimajor axis a, proper frequency of the orbital plane precession in the inertial space s, proper inclination $I_{\rm p}$, proper longitude of node $\Omega_{\rm p}$ at J2000.0 (i.e., phase of the proper term in Fourier representation of the osculating non-singular inclination vector $\sin I/2 \exp(\imath\Omega)$), forced inclination associated with s_6 frequency I_6, and forced longitude of node Ω_6 at J2000.0 (i.e., phase of the s_6 term in Fourier representation of the osculating non-singular inclination vector $\sin I/2 \exp(\imath\Omega)$).

[b] The s_6 spectral line is not well resolved in this case since there is power in a broader zone about its value.

With two spectral lines in $\sin I/2 \exp(\imath\Omega)$ we introduce Cassini resonance variables that are associated with the two frequencies s and s_6 (from here on, we call them the s and s_6 resonances). The resonant obliquity is just the angular distance of the instantaneous orientation of the spin axis from normal of each of the precessing reference frames defined by spectral terms in $\sin I/2 \exp(\imath\Omega)$. The critical angles of each of the resonances are defined as in Section 2, namely, $\phi = -(\psi + \Omega)$, where Ω is the nodal longitude of the corresponding term in the inclination vector (see also Appendix A). Figs. 4 and 5 show surfaces-of-section (SOSs) for a number of orbits shown in the plane of resonant obliquity ϵ_s and associated critical angle ϕ_s of the s resonance when the critical angle of the s_6 resonance is null and its time derivative is positive. Each orbit was started at $\phi_s = 0°$ and was given different values of ϵ_s. We computed SOS not only for the nominal parameters of Gaspra's rotation state (bottom and right in Fig. 4) but also for modified values of Gaspra's rotation period (shorter in previous panels of Fig. 4 and longer in Fig. 5). This approach was repeated for all of the cases discussed in Sections 3.2–3.5.

We first discuss the results for our nominal parameters. The SOS is composed of two regions with qualitatively different be-

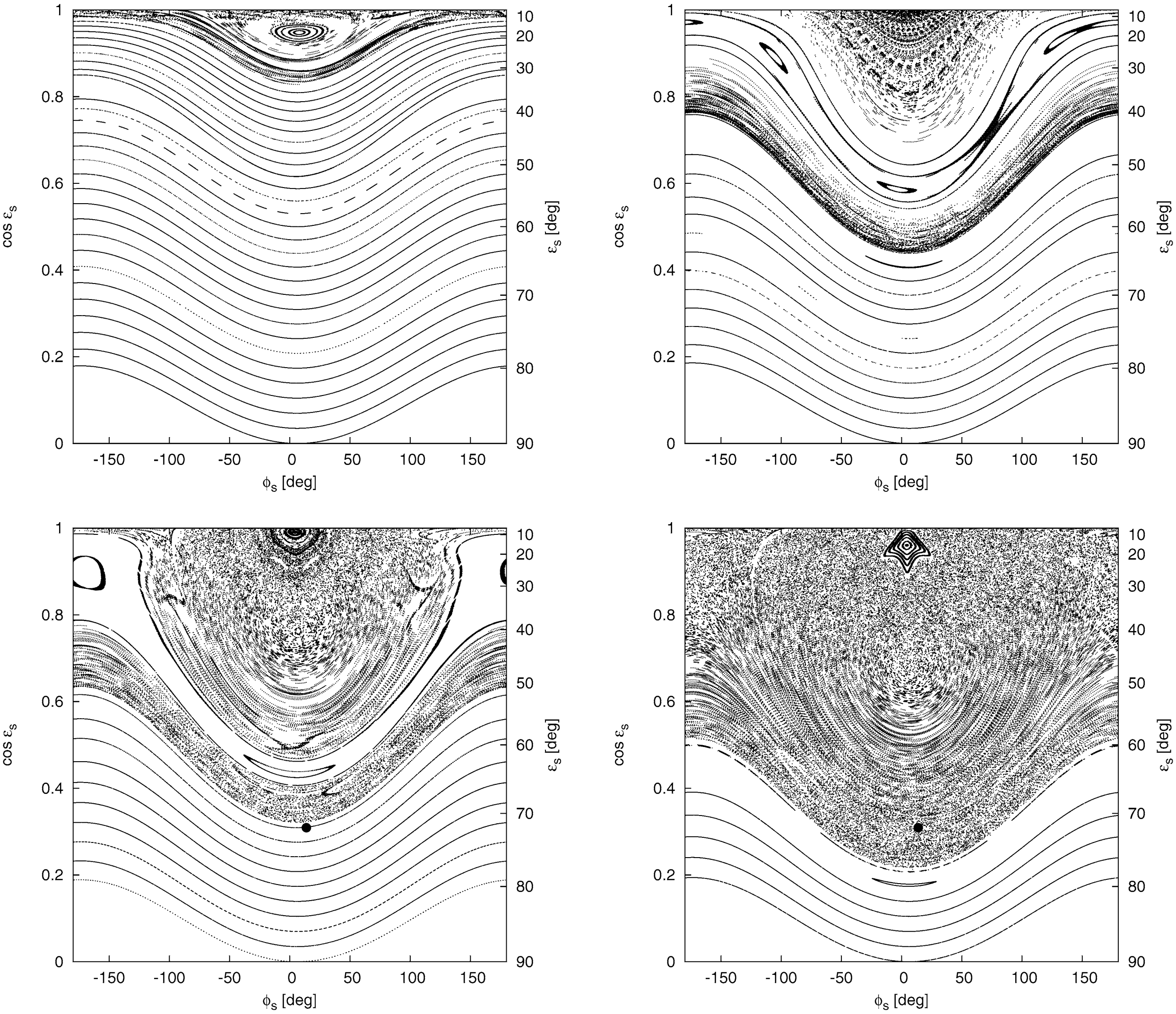

Fig. 4. Surfaces-of-section for a toy model consisting of only two spectral lines—proper s and forced s_6—in Gaspra's non-singular inclination vector $\sin I/2 \exp(\imath\Omega)$. Amplitudes and phases of all necessary terms are taken from numerical integration. Here we show the spin axis evolution in the variables of the proper mode—proper obliquity ϵ_s and the critical angle of the s spin–orbit resonance ϕ_s—when the critical angle of the s_6 spin–orbit resonance is zero and its time derivative positive. Different panels for different (modified) values of Gaspra's rotation period: (i) top left—$P = 0.5P_{\rm Gaspra}$ (where $P_{\rm Gaspra} = 7.04$ h is the observed value), (ii) top right—$P = 0.75P_{\rm Gaspra}$, (iii) bottom left—$P = 0.85P_{\rm Gaspra}$, and (iv) bottom right—$P = P_{\rm Gaspra}$. The last panel thus corresponds to the nominal Gaspra situation. The symbol in the last two panels indicates current position of Gaspra's spin axis in the same variables.

havior: (i) for small values of ϵ_s (top of figures), we observe a large chaotic zone triggered by an overlap of the s and s_6 resonances, and (ii) for large values of ϵ_s (bottom of figures), the motion becomes quasi-regular. The current position of Gaspra's pole in these variables—$\epsilon_s \simeq 72°$ and $\phi_s \simeq 14°$—places it at the border of the chaotic zone. Rubincam et al. (2002), who were the first to notice this feature, found that Gaspra's obliquity can wander over a large range of values from 0° to nearly 75°. Note there is no stable island of quasi-regular orbits left near the Cassini state 2 of the s resonance (the structure at $\epsilon_s \simeq 15°$ is associated with one of the secondary resonances). We therefore predict that the long-term evolution of Gaspra's spin axis is highly irregular at present.

The purpose of computing SOSs for modified values of Gaspra's rotation period is that this parameter is secularly affected by the YORP torques. Over long time periods, the individual SOSs seen in Figs. 4 and 5 might only be snapshots of Gaspra's spin axis behavior at that particular value of its period. Obviously, YORP-induced changes of the rotation period depend on the history of Gaspra's obliquity (e.g., Rubincam, 2000; Vokrouhlický and Čapek, 2002), with a complicated feedback taking place between the two parameters. We shall study this process in Section 4. Here we only note that for sufficiently small values of P ($\simeq$4 h; Fig. 4), the chaos is limited because the s resonance ceases to exist; the s_6 resonance is the only one left behind. If Gaspra's rotation period were reduced to 6 h (bottom left panel in Fig. 4), it would place the current pole position out of the chaotic zone, which in turn would make its obliquity evolution much more regular. This explanation is consistent with numerical results shown in Rubincam et al. (2002). Longer P values for Gaspra lead to a more limited chaotic zone (Fig. 5) because widths of the s and s_6 resonances both shrink

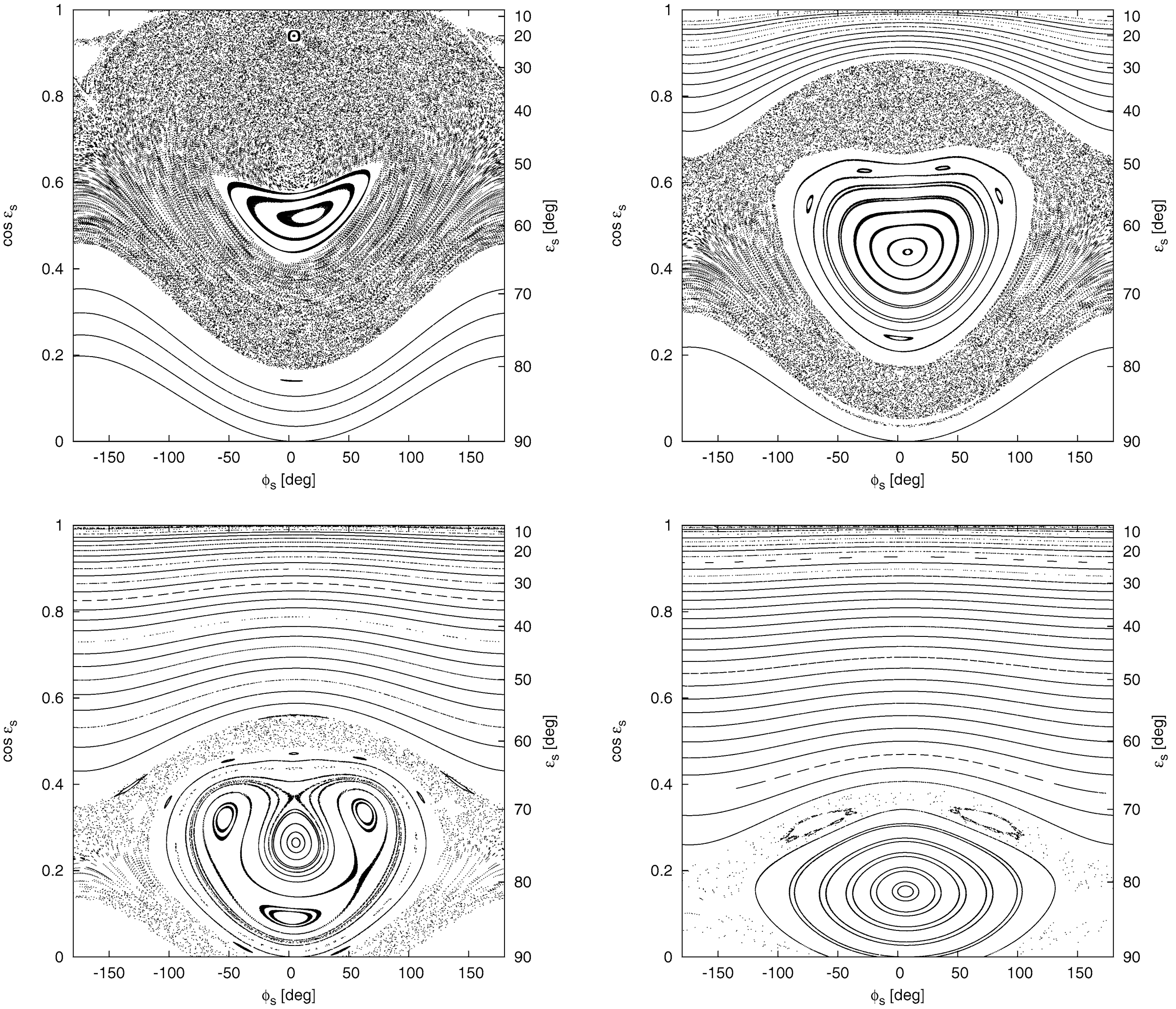

Fig. 5. Continuation of Fig. 4 now for the following rotation period values: (i) top left—$P = 1.1 P_{\mathrm{Gaspra}}$, (ii) top right—$P = 1.5 P_{\mathrm{Gaspra}}$, (iii) bottom left—$P = 3 P_{\mathrm{Gaspra}}$, and (iv) bottom right—$P = 5 P_{\mathrm{Gaspra}}$.

and migrate close to 90° obliquity (see Appendix A). Stable librations about Cassini state 2 then become possible (note also the pronounced effect of the 3/1 secondary resonance when $P = 3 P_{\mathrm{Gaspra}}$; this feature, however, seems to disappear in our full numerical model below where we included all frequencies in the inclination vector). Reviewing these results, we conclude that Gaspra's obliquity is currently in its most violent evolution phase.

To check the results presented above, we propagated Gaspra's spin axis parameters into the future using the Euler equation (12) (and $\boldsymbol{\tau}^\star = 0$) as well as a full representation of Gaspra's orbit precession. Fig. 6 shows the evolution of the osculating obliquity during the next 50 My. A timestep of 200 yr was used (i.e., the same value was used in all of the rest of our numerical simulations). Here the large-scale variations of Gaspra's obliquity and its chaotic nature are easily seen. The bottom panels of Fig. 6 show that the critical angles of both the s and s_6 resonances temporarily librate, but their mutual interaction prevents them from entering into a long-term, stable libration regime. At the end of the integration timespan, the spin axis detaches from the s resonance and becomes more stable in a higher obliquity regime. Fig. 7 confirms that this interesting behavior is reasonable. Gaspra's spin trajectory is projected onto the plane of resonance variables ϵ_s and ϕ_s, with the left panel the SOS of the simplified two-frequency model while the right panel is the relevant projection of the complete solution. We note the real orbit nearly-uniformly fills the same zone as predicted by the two-frequency model, with only minor extension.

Our results were found to be robust against small changes in Gaspra's spin and orbital integration data, even though the orbit of Gaspra is chaotic with a Lyapunov characteristic timescale of ≃100 ky (e.g., http://newton.dm.unipi.it/). We found that while our alternative solutions (such as the obliquity's dependence on time) diverged on a 0.1–1 My timescale, they remained qualitatively the same. In some cases, Gaspra's spin axis left the s resonance zone in order to enter into temporarily-stabilized conditions at higher obliquities (such as at the end of the nominal simulation in Fig. 6) before again being captured by the resonance.

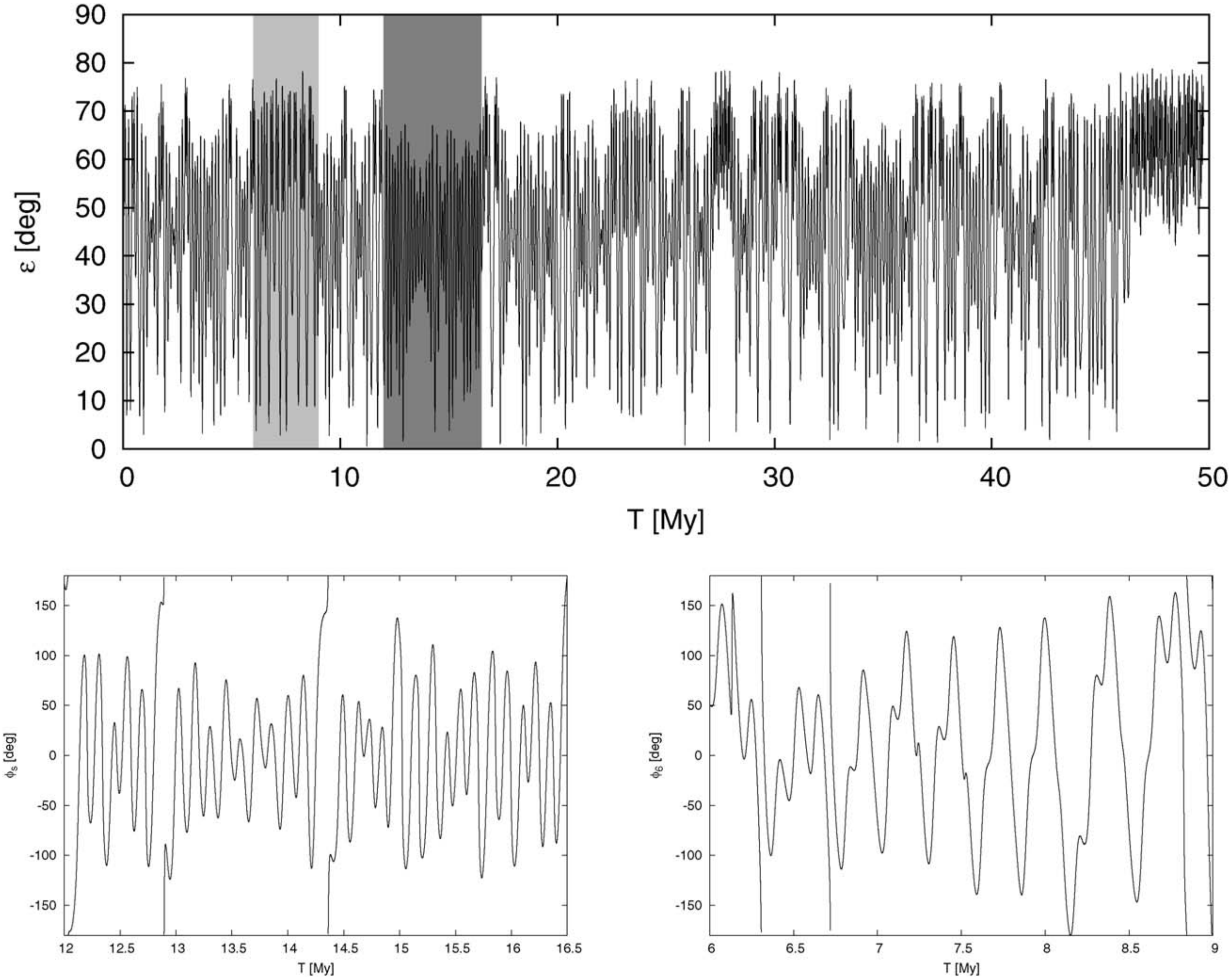

Fig. 6. Gaspra's spin integration over 50 My time interval. Upper panel shows osculating obliquity as a function of time. The evolution is characterized by intermittent librations and circulations about the Cassini state 2 of both s and s_6 resonances. The shaded intervals point out temporary libration stages: (i) the s resonance (also bottom left) and (ii) the s_6 resonance (also bottom right). The bottom figures show behavior of the critical angle of both resonances—ϕ_s for the s resonance and ϕ_6 for the s_6 resonance—during their prevailing librations. YORP torques are not included in this simulation.

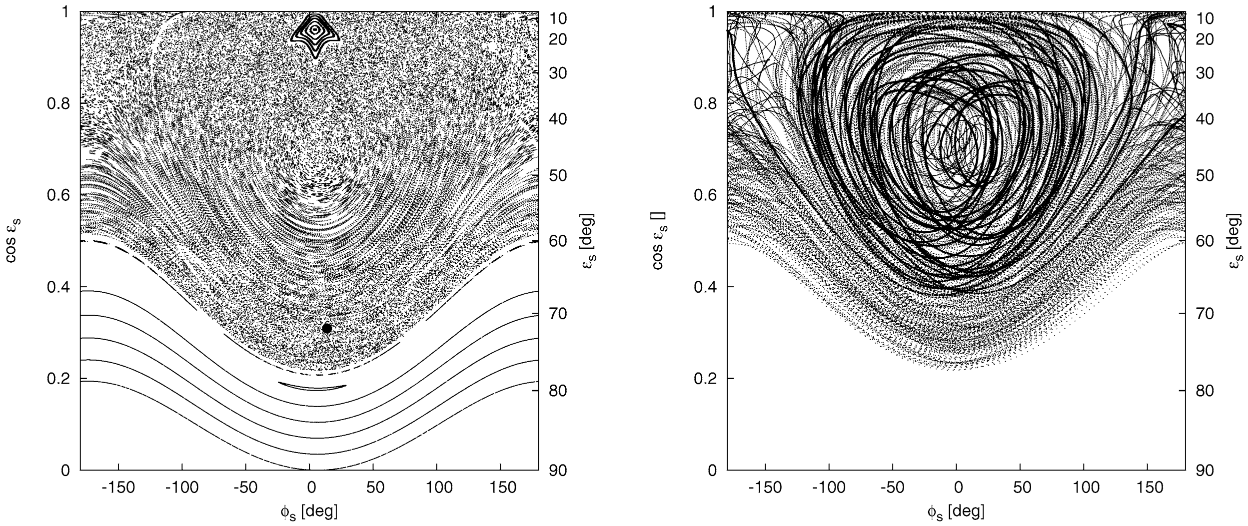

Fig. 7. Left: Surface-of-section for a toy model consisting of only two spectral lines in the Gaspra's orbit non-singular inclination vector $\sin I/2 \exp(\iota \Omega)$—proper s and the forced s_6. Amplitudes and phases taken from numerical analysis of the Gaspra's orbit. Axes as in Fig. 4. Right: Gaspra's spin integration over 50 My time interval projected onto the plane of resonant variables of the s secular spin–orbit resonance. The bold section of the trajectory is the period shown in the light-shaded box in Fig. 6 when the spin predominantly librates in the (ϵ_s, ϕ_s) plane.

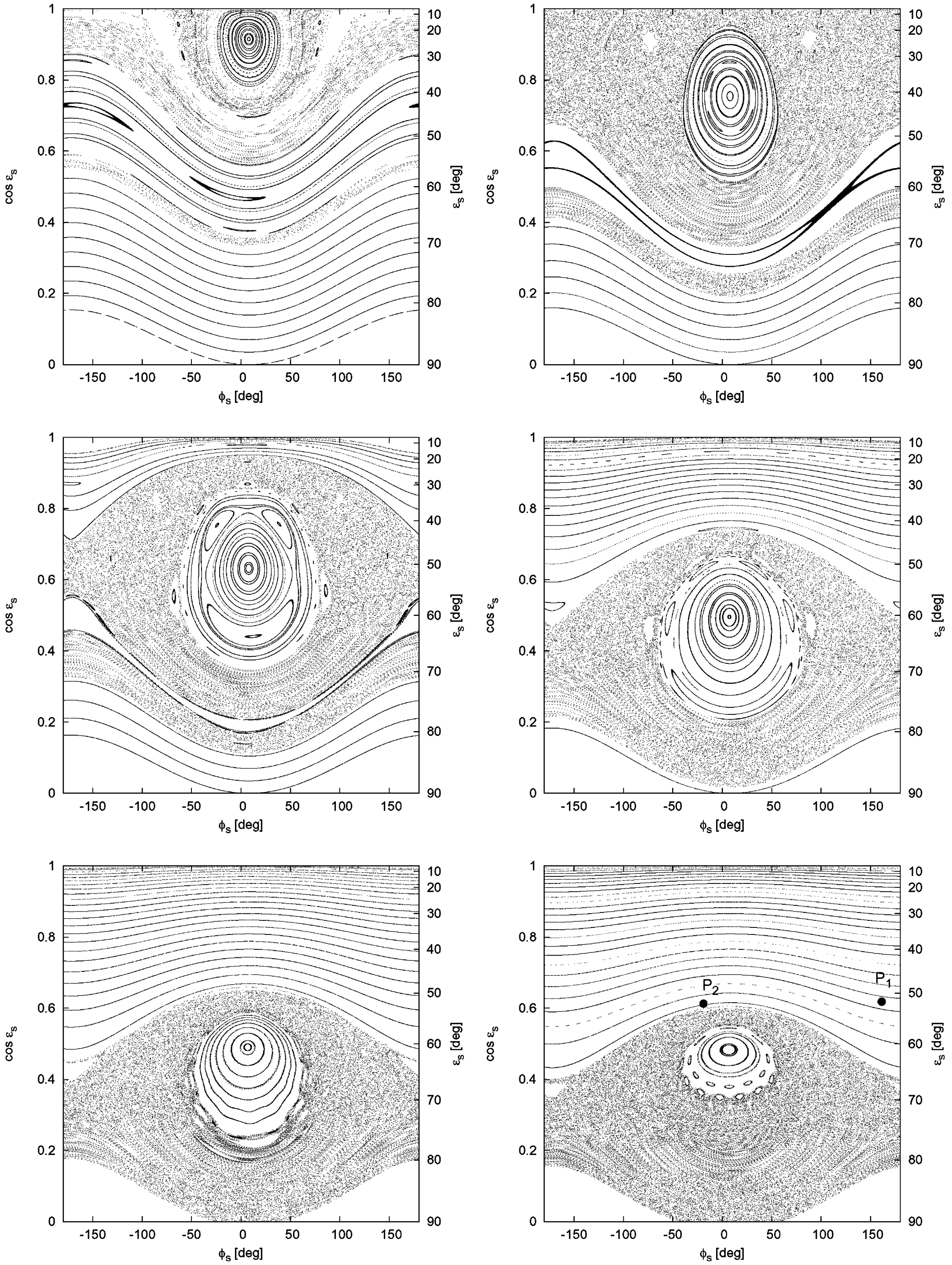

Fig. 8. Surface-of-section for a toy model consisting of only two spectral lines in the Echo's orbit non-singular inclination vector $\sin I/2 \exp(\imath\Omega)$—proper s and the forced s_6. Amplitudes and phases taken from numerical analysis of Echo's orbit. Different panels for different (modified) values of Echo's rotation period: (i) top left—$P = 0.3P_{\rm Echo}$ (where $P_{\rm Echo} = 25.2$ h is the observed value), (ii) top right—$P = 0.4P_{\rm Echo}$, (iii) middle left—$P = 0.5P_{\rm Echo}$, and (iv) middle right—$P = 0.75P_{\rm Echo}$, (iv) bottom left—$P = 0.9P_{\rm Echo}$, and (v) bottom right—$P = P_{\rm Echo}$. The two symbols P_1 and P_2 are pole solutions by Michałowski (1993).

This analysis supports and actually explains in greater detail an earlier suggestion by Rubincam et al. (2002) that large variations in Gaspra's obliquity is related to proximity to the s resonance (somewhat incorrectly called "the obliquity resonance" by these authors). In Section 4, however, we take issue with their conclusion that this configuration can be considered positive evidence that YORP has influenced the evolution of the spin state (i.e., we agree that YORP has likely affected Gaspra's spin state, but proving it using current data is challenging).

3.2. (60) Echo

Unlike (951) Gaspra, all of our other test asteroids are not members of any asteroid family. This implies their past spin

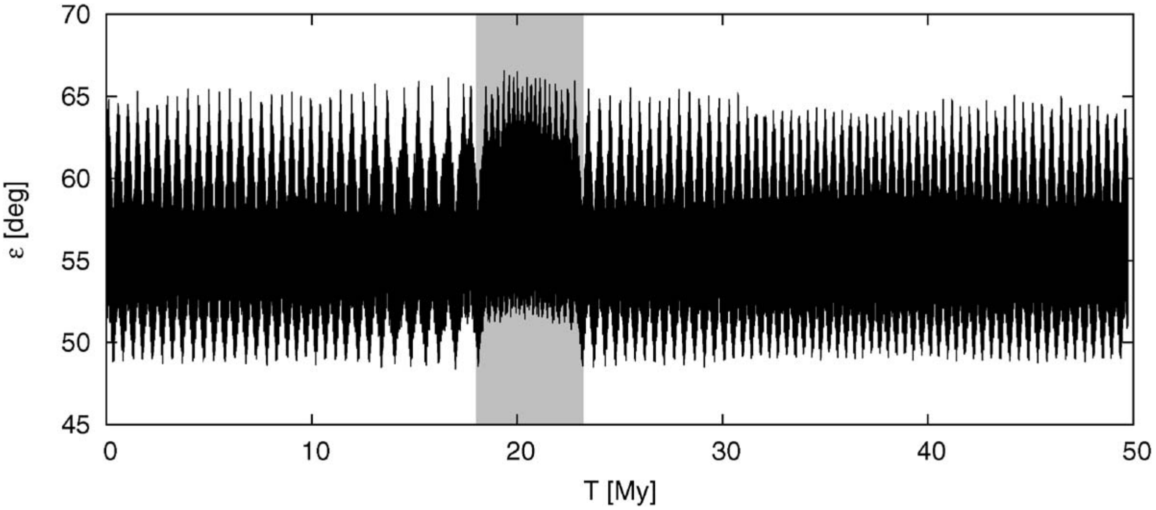

Fig. 9. Echo's spin integration over 50 My time interval. The evolution is fairly regular as compared to the Gaspra's case (Fig. 6), mostly because the spin–orbit resonances are located at higher obliquity due to Echo's anomalously slow rotation. A weak chaos, documented by the behavior in between 18 and 23 My (shaded zone), is related to a tiny resonance associated to the $\simeq -58$ arcsec/yr precession frequency of Echo's orbital plane which produces a chaotic layer sticked to the separatrix of the s resonance. YORP torques are not included in this simulation.

evolution could be as long as >4 Gy. We will use this information in Section 4. (60) Echo, $a \simeq 60$ km size asteroid (Tedesco et al., 2002) with osculating orbital elements of semimajor axis $a = 2.39$ AU, eccentricity $e = 0.184$, and inclination $I = 3.59°$, resides at a somewhat larger heliocentric distance than Gaspra (Fig. 3) while having about the same orbital inclination. Michałowski (1993) determined the following parameters of the rotation state of this asteroid: rotation period $P = 25.15$ h, and two possible pole orientations P_1: $(\ell, b) = (95°, 34°)$ and P_2: $(\ell, b) = (275°, 42°)$. We use the axes-ratio of the best matching ellipsoid from the same reference to estimate Echo's value of $\Delta \simeq 0.34$. There is considerable uncertainty in this value, but we use it for the sake of our numerical experiment. Below we use the same diagnostic techniques to investigate Echo's spin axis evolution as in Section 3.1; some of Echo's orbital data are given in Table 1.

Fig. 8 shows SOSs computed for nominal and modified values of Echo's rotation period P. Because P is already large, we also investigate here cases where P was smaller. We see similar behavior in Fig. 8 as that for Gaspra (Figs. 4 and 5), namely as P decreases, the s resonance migrates toward smaller obliquity values and covers a broader zone until it disappears at $P \simeq 10.2$ h. For Echo's nominal parameters, both pole solutions are located inside the stable zone of the s resonance and hence the obliquity evolution of Echo's spin axis is expected to be more regular than in Gaspra's case. The pole solution P_2 is closer to the separatrix of the s resonance, which is why we choose it for the numerical investigation described below (the solution for P_1 would be even more stable). In passing, we note that contrary to previous experience with Gaspra, the stable libration zone about the Cassini state 2 shrinks in size over the last two panels of Fig. 8. We hypothesize that the extended chaos zone is triggered by the chain of secondary resonances that terminate the regular zone in these two last panels. Another interesting feature is the quasi-stable layer that intersects the chaotic zone in the first three panels at large obliquity values. This is the stable libration zone of the s_6 resonance projected onto the resonant variables of the s resonance.

Fig. 9 confirms the quasi-regularity of Echo's obliquity evolution over a 50 My time interval. The anomalous behavior between 18 and 23 My, however, suggests there is more complexity in the full numerical experiment than in the two-frequency model. We found the highlighted feature is caused by the presence of a *third line* in the Fourier representation of the nonsingular inclination vector $\sin I/2 \exp(\imath \Omega)$ that has a frequency $\simeq -58.2$ arcsec/yr. In spite of the small forced inclination of $\simeq 0.23°$ associated with this line, it produces a thin chaotic layer that adheres to the separatrix of the s resonance. In our numerical experiment, Echo's spin axis was temporarily confined to this chaotic zone between 18 and 23 My. In Section 4.2, we constructed a toy model showing how this tiny additional resonance may have significantly affected Echo's past spin evolution. Thus, the take away message from these results are that the spin evolution of asteroids in the inner main belt can be remarkably complex.

3.3. *(32) Pomona*

Asteroid (32) Pomona, with osculating $a = 2.59$ AU, $e = 0.086$, and $I = 5.52°$, is the most distant asteroid examined in this paper. It resides in the central main asteroid belt (Fig. 3). This $D \simeq 80$ km asteroid (Tedesco et al., 2002) has been extensively observed, allowing Kaasalainen et al. (2002) to unambiguously determine its rotation-state parameters: $P = 9.45$ h, $(\ell, b) = (267°, 58°)$. This shape model indicates $\Delta \simeq 0.28$, somewhat less elongated than in the previous two cases.

Fig. 10 shows the SOSs for the nominal parameters of Pomona's rotation state (top right), together with five more cases corresponding to smaller and larger P values. Because Pomona has an increased proper precession rate of the orbital plane ($s = -50.6$ arcsec/yr; Table 1), and a comparably small value of Δ, the s resonance about Cassini state 2 only bifurcates

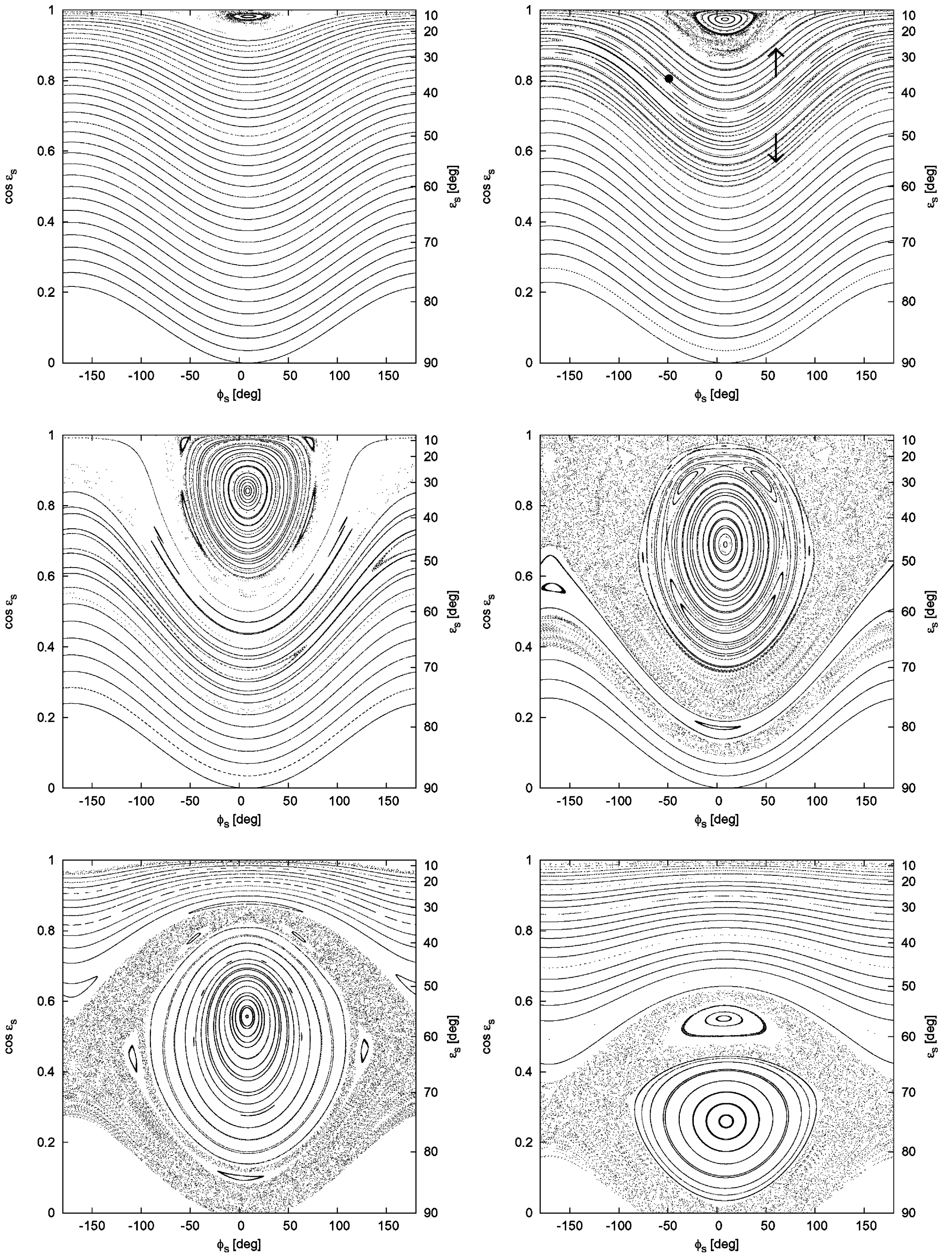

Fig. 10. Surface-of-section for a toy model consisting of only two spectral lines in the Pomona's orbit non-singular inclination vector $\sin I/2 \exp(\imath \Omega)$—-proper s and the forced s_6. Amplitudes and phases taken from numerical analysis of the Pomona's orbit. Different panels for different (modified) values of Pomona's rotation period: (i) top left—$P = 0.5 P_{\mathrm{Pomona}}$ (where $P_{\mathrm{Pomona}} = 9.45$ h is the observed value), (ii) top right—$P = P_{\mathrm{Pomona}}$, (iii) middle left—$P = 1.5 P_{\mathrm{Pomona}}$, and (iv) middle right—$P = 2 P_{\mathrm{Pomona}}$, (iv) bottom left—$P = 3 P_{\mathrm{Pomona}}$, and (v) bottom right—$P = 5 P_{\mathrm{Pomona}}$. The s resonance does not exist in the first three panels; the arrows in the nominal case indicate width of the s_6 resonance projected onto the variables used here and the symbol is a pole position derived by Kaasalainen et al. (2002).

when the P value exceeds its current value by a factor of 2. Thus, the nominal spin dynamics of Pomona is not affected by the s resonance. Instead, it resides closely to the s_6 resonance.

This result is confirmed by Fig. 11, which shows what happens when we numerically propagate Pomona's spin axis forward 50 My. The evolution of its obliquity, which overall is quasi-regular, undergoes intermittent excursions toward larger values forced by the s_6 resonance. Moreover, the proper inclination is large enough ($I \simeq 6.1°$) that the orbit only temporary visits the libration zone of the s_6 resonance. A better exam-

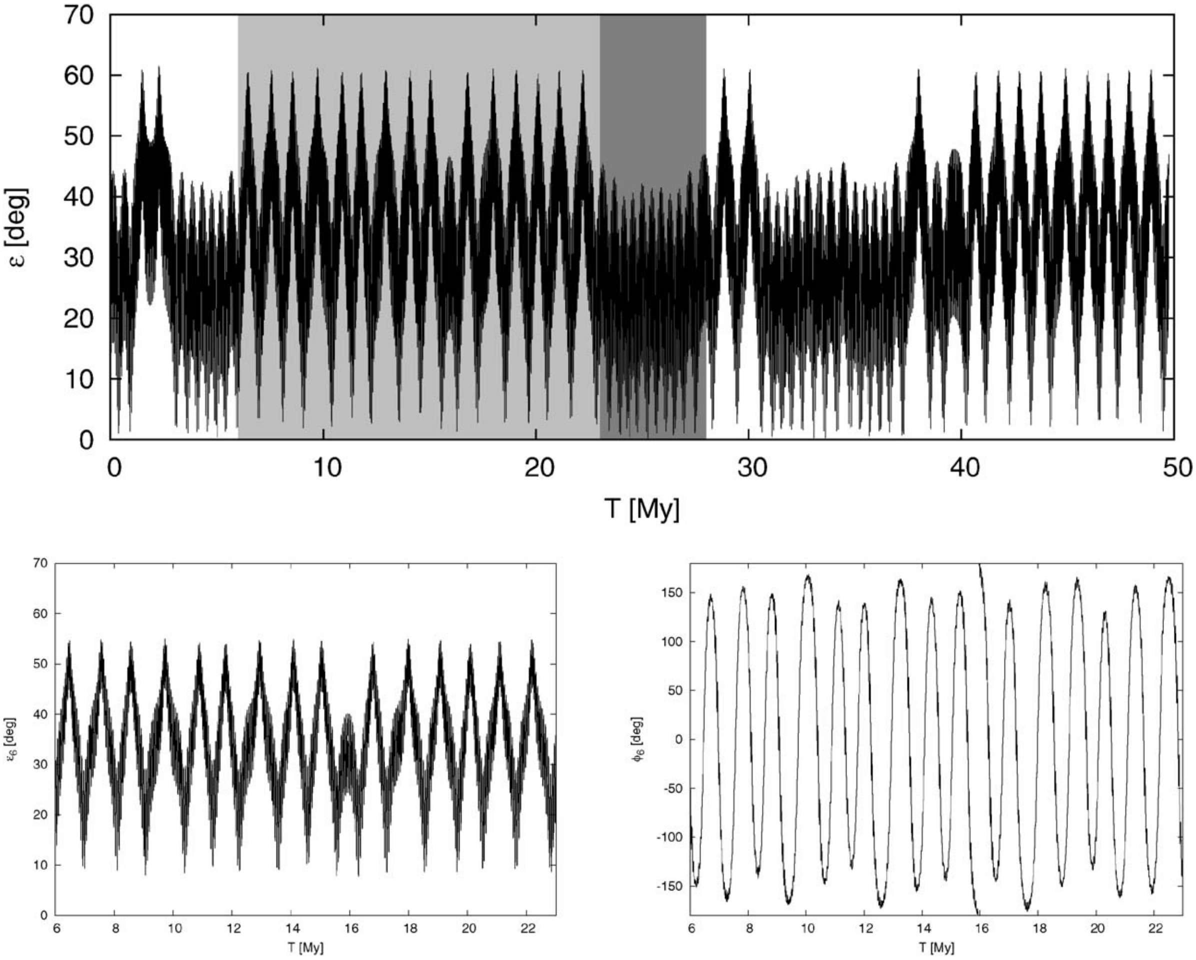

Fig. 11. Pomona's spin integration over 50 My time interval. Obliquity evolution is much more regular than in the inner part of the main belt, mainly because of absence of the Cassini resonance associated with the s frequency. The high-obliquity excursions (ligth shaded and zoomed in bottom figures) mark large amplitude librations about the s_6 resonance, while the low-obliquity mode (dark shaded) occurs during circulation above the s_6 resonance. The bottom figures show behavior of the resonant obliquity ϵ_6 and resonant angle ϕ_6 during the libration phase. YORP torques are not included in this simulation.

ple of this behavior is seen in Fig. 12, where the evolution is projected onto the plane of resonant variables associated with the s_6 frequency in $\sin I/2 \exp(\imath \Omega)$. Interestingly, the spin axis occasionally performs a large amplitude libration in the s_6 resonance while mostly staying outside this resonance in a region characterized by a smaller obliquity. The shorter period superimposed on the large obliquity oscillations ($\sim 12°$) are just the geometric (but not resonant) effect of the proper term in $\sin I/2 \exp(\imath \Omega)$.

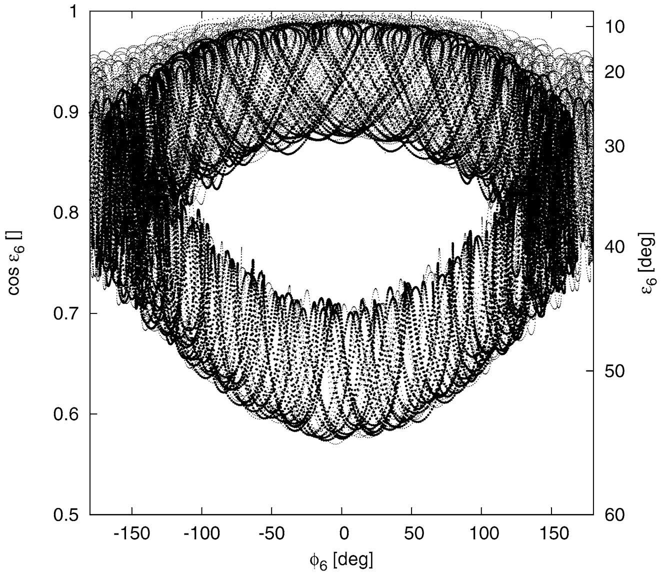

Fig. 12. Pomona's spin integration over 50 My time interval (dots) projected onto the plane of resonant variables of the s_6 spin–orbit resonance. The bolt section is a 17 My segment between time 6 and 23 My, when the Pomona axis resides librating about the Cassini state 2 (see also Fig. 11).

3.4. (230) Athamantis

With (320) Athamantis, we shift toward exploring spin history for asteroids residing on higher-inclination orbits, although the proper inclination of this case—$I \simeq 10.2°$—is still close to the average in the main-belt. For reference, it has osculating $a = 2.38$ AU, $e = 0.06$, and $I = 9.43°$. Torppa et al. (2003) collected available lightcurve observations and determined a rotation period $P = 23.98$ h and two possible pole solutions: P_1 with $(\ell, b) = (74°, 28°)$ and P_2 with $(\ell, b) = (238°, 27°)$. Here we use P_2 for our analysis but P_1 yields comparable results. A mild elongation for this $D \sim 110$ km asteroid yields an

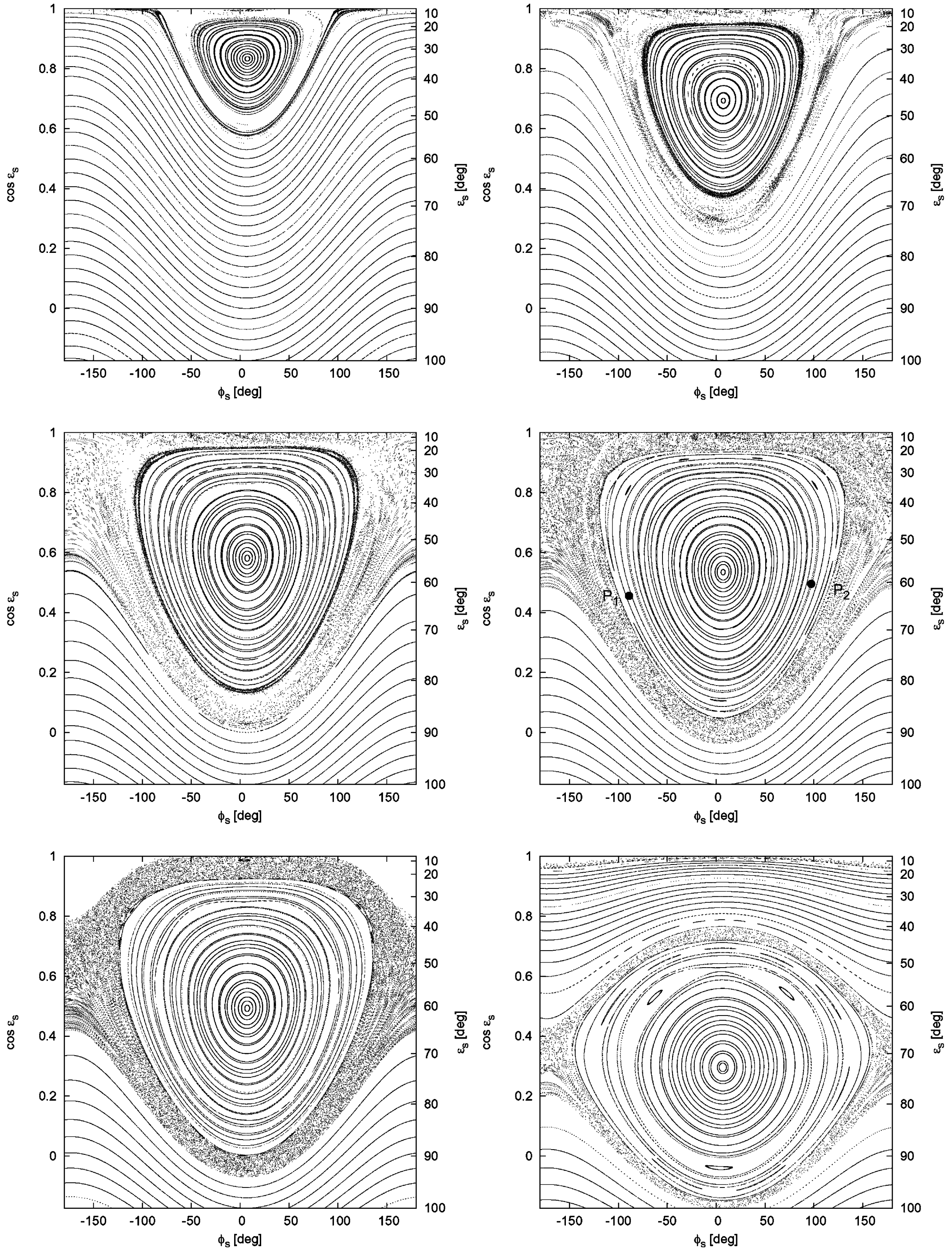

Fig. 13. Surface-of-section for a toy model consisting of only two spectral lines in the Athamantis' orbit non-singular inclination vector $\sin I/2 \exp(\imath\Omega)$—proper s and the forced s_6. Amplitudes and phases taken from numerical analysis of the Athamantis' orbit. Different panels for different (modified) values of Athamantis' rotation period: (i) top left—$P = 0.5 P_{\mathrm{Athamantis}}$ (where $P_{\mathrm{Athamantis}} = 24$ h is the observed value), (ii) top right—$P = 0.7 P_{\mathrm{Athamantis}}$, (iii) middle left—$P = 0.9 P_{\mathrm{Athamantis}}$, and (iv) middle right—$P = P_{\mathrm{Athamantis}}$, (iv) bottom left—$P = 1.1 P_{\mathrm{Athamantis}}$, and (v) bottom right—$P = 2 P_{\mathrm{Athamantis}}$. The two symbols P_1 and P_2 are pole positions determined by Torppa et al. (2003).

approximate value of $\Delta \simeq 0.15$, but we caution that the uncertainty in this value is large.

Fig. 13 gives SOSs for various P values of Athamantis. In spite of its small Δ value, the slow rotation makes $\xi = \Delta P_6$ large enough that both s_6 and s resonances exist at the same time (middle right). The s resonance is broad and even partially extends into the retrograde rotation zone. This is expected because the resonance width scales as $W \propto \sqrt{\sin I}$ (e.g., Eq. (A.2)). The width of the s_6 resonance is more limited because the forced inclination I_6 is roughly the same throughout the main belt (see also Table 1). This in turn makes the s resonance less perturbed. Overall, the variety of possible motions

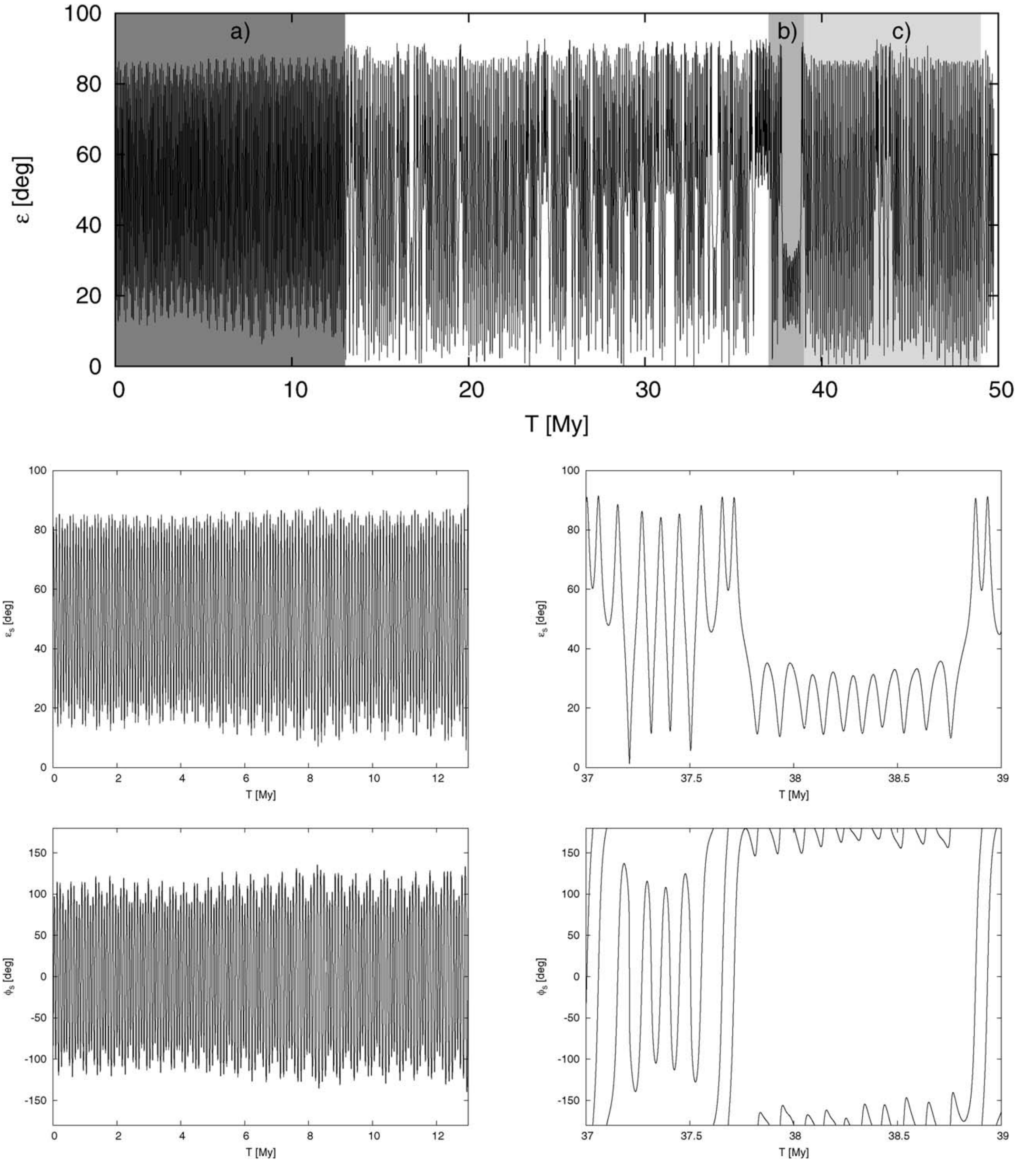

Fig. 14. Athamantis' spin integration over 50 My time interval. The shaded intervals indicate (from left to right): (a) initial period of librations about the Cassini state 2 of the s resonance, (b) temporary capture to another stable point associated with the s resonance at $\phi_s \sim 180°$ (alike the Cassini state 1) but with much smaller stability zone, and (c) temporary capture to the s_6 resonance (see also Fig. 15). Phases (a) and (b) of various librations in the s resonance are zoomed in the middle and bottom panels. YORP torques are not included in this simulation.

are less irregular for Athamantis because the chaotic layer is confined to a region near its separatrix. This means that a large zone of quasi-regular libration about Cassini state 2 is possible.

Both of Athamantis' pole solutions are located near the edge of these regular/chaotic zones. This makes their evolution nearly identical. Except when Athamantis has a slow rotation rate and a small obliquity, which ties the spin vector to the precessing orbit, the variations of Athamantis' obliquity values are always large. In part, this is caused by strong resonance effects. Even when the s resonance does not exist (e.g., the first two panels in Fig. 13), however, the obliquity still oscillates at $\geqslant 2I \sim 20°$ amplitude for geometric reasons.

Figs. 14 and 15 show results where we numerically tracked the evolution of Athamantis' spin vector over 50 My. As ex-

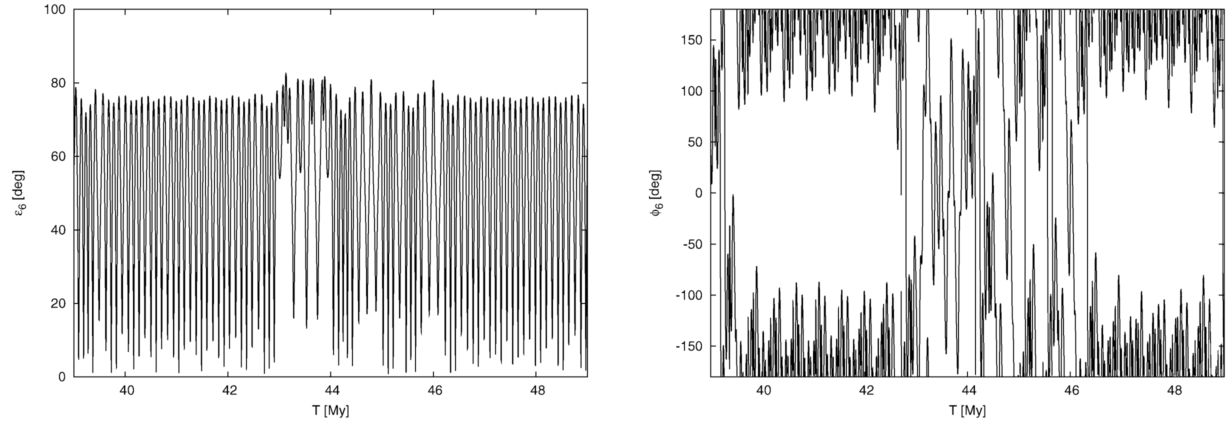

Fig. 15. Athamantis' spin axis evolution in between 39–49 My—interval (c) in Fig. 14—when the spin axis undergoes anomalous oscillations in the s_6 resonance: (i) left is the obliquity in the s_6 resonance reference frame, (ii) right is the critical angle of the s_6 resonance. Oscillations occur about the $\phi_6 = 180°$ center.

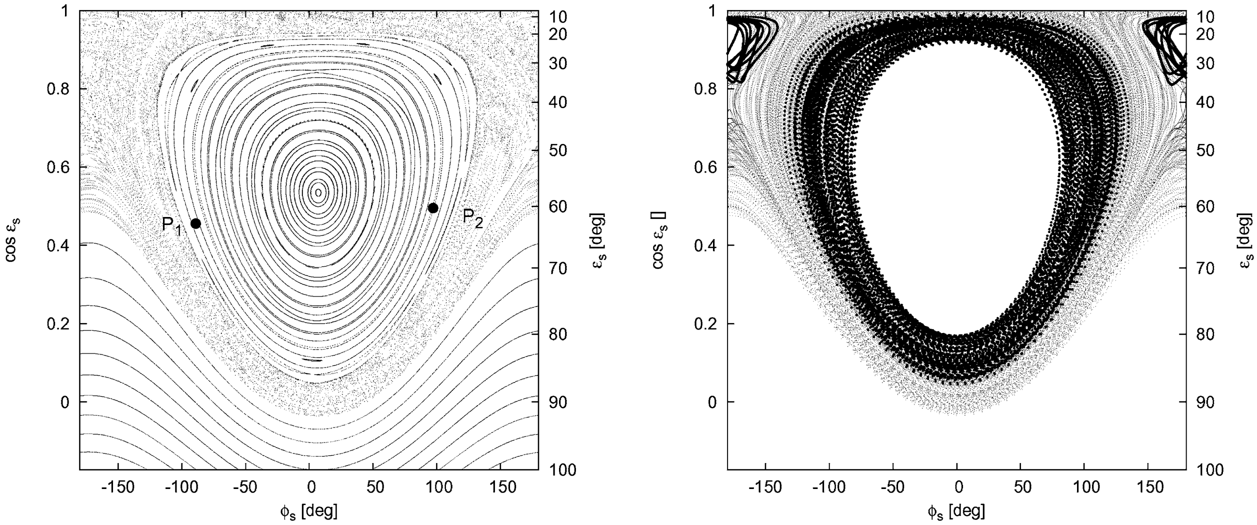

Fig. 16. Left: Surface-of-section for a toy model consisting of only two spectral lines in the Athamantis' orbit non-singular inclination vector $\sin I/2 \exp(\imath\Omega)$—proper s and the forced s_6. Amplitudes and phases taken from numerical analysis of the Athamantis' orbit. Right: Athamantis' spin integration over 50 My time interval (dots) projected onto the plane of resonant variables of the s secular spin–orbit resonance. The bolt sections show: (i) the initial libration about $\phi_s \sim 0°$ ("regular position of the Cassini state 2" shown as (a) in Fig. 14) during the first 10 My of the simulation, and (ii) temporary oscillation about the new stable point near $\phi_s \sim 180°$ (shown as (b) in Fig. 14).

pected, the first 12 My show large obliquity oscillations, but a closer inspection reveals a number of intricate dynamical effects likely related to the fact that the power spectrum of the non-singular inclination vector $\sin I/2 \exp(\imath\Omega)$ contains many more lines than the two used in our simplified model. For instance, we note that both periods of normal libration about the Cassini state 2 of the s resonance (Fig. 14 left bottom panels) and also an anomalous oscillation about stable point at $\phi_s = 180°$ about Cassini state 1 (Fig. 14 right bottom panels). Similarly, Fig. 15 shows a long-lasting period of oscillation about an anomalous stable point in the s_6 resonance. Both features are also shown in Fig. 16, where they are compared to previous SOS for Athamantis' nominal rotation parameters. The two-line model seem to prohibit oscillations about the Cassini state 1, but surprisingly the full numerical integration treatment allows it. We also note that the extension of the stable libration zone about the Cassini state 2 is somewhat reduced in the full model as compared to the two-line model, perhaps as a result of perturbations by other spectral lines in $\sin I/2 \exp(\imath\Omega)$.

3.5. (105) Artemis

Asteroid (105) Artemis is the largest ($D \sim 110$ km size) member of the Phocaeas, a dynamical group of asteroids characterized by high-inclination orbits. It has osculating $a = 2.37$ AU, $e = 0.18$, and $I = 21.5°$. The proper inclination of its orbit, $I_{\rm p} \simeq 21.6°$ (see Table 1), is high enough that we expect significant variations should occur in its spin orientation with respect to the orbit. Tungalag et al. (2002) obtained the following solution for this asteroid's rotation state: $P = 18.55$ h and pole position $(\ell, b) = (192°, 68°)$. Axes-ratio of the best-fitting ellipsoid suggests $\Delta \simeq 0.30$, though we caution there is considerable uncertainty in this value. Tests indicate, however, that even a 30% reduction in Δ does not significantly affect our results.

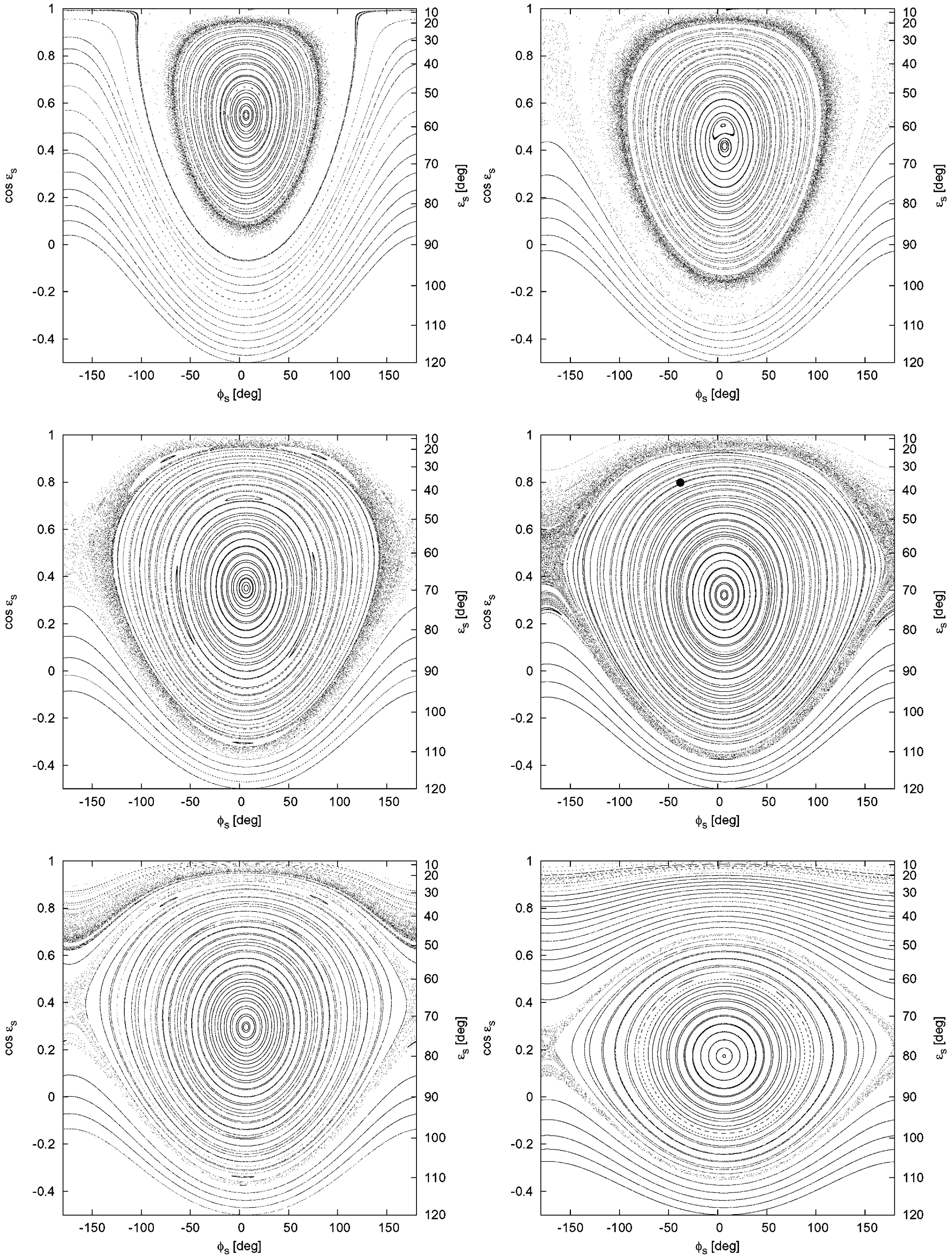

Fig. 17. Surface-of-section for a toy model consisting of only two spectral lines in the Artemis' orbit non-singular inclination vector $\sin I/2\exp(\imath\Omega)$—proper s and the forced s_6. Amplitudes and phases taken from numerical analysis of the Artemis' orbit. Different panels for different (modified) values of Artemis' rotation period: (i) top left—$P = 0.5P_{\mathrm{Artemis}}$ (where $P_{\mathrm{Artemis}} = 18.6$ h is the observed value), (ii) top right—$P = 0.7P_{\mathrm{Artemis}}$, (iii) middle left—$P = 0.9P_{\mathrm{Artemis}}$, and (iv) middle right—$P = P_{\mathrm{Artemis}}$, (iv) bottom left—$P = 1.1P_{\mathrm{Artemis}}$, and (v) bottom right—$P = 2P_{\mathrm{Artemis}}$. The symbol is a pole position by Tungalag et al. (2002).

Fig. 17 shows SOSs for Artemis' nominal and slightly modified rotation rate. As soon as the s resonance bifurcates (roughly the upper right panel), it essentially covers all of the prograde states and even a fair portion of the retrograde ones. It is no surprise, then, that the current pole position for Artemis' falls inside the libration zone of the s resonance. The s_6 resonance triggers chaos in a restricted region near the separatrix of the s resonance within two-spectral-line model. Most of the initial conditions result in quasi-regular motion, either libration or circulation in the s resonance.

A full-fledged numerical simulation of the Artemis' spin evolution (Figs. 18 and 19), however, indicates that more chaos is present than suggested by the two frequency model, presumably because the Fourier spectrum of $\sin I/2\exp(\imath\Omega)$ is

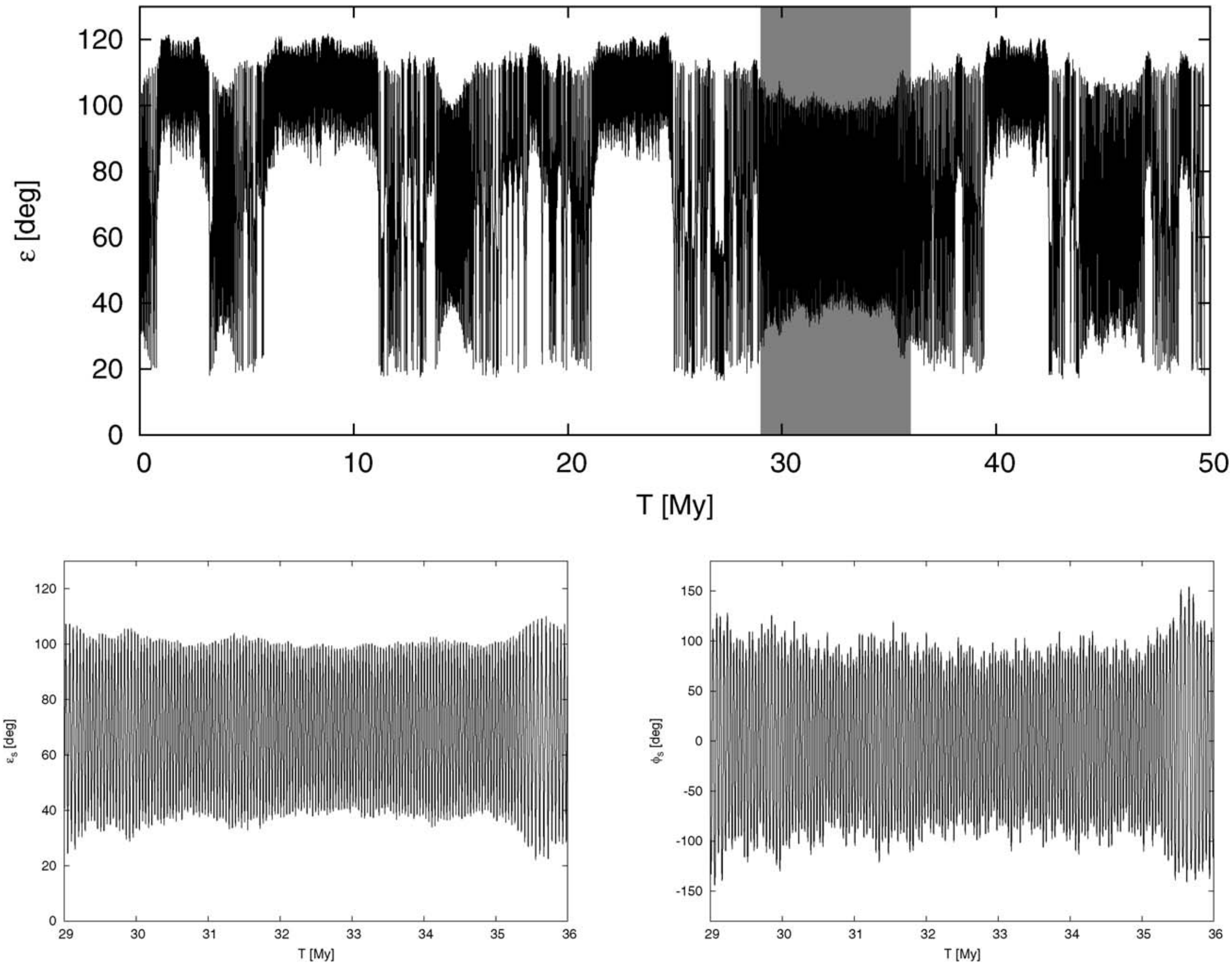

Fig. 18. Artemis' spin integration over 50 My time interval. Shaded interval points to a temporary capture in the libration zone about the Cassini state 2 of the s resonance. Bottom panels show behavior of the resonance obliquity ϵ_s and resonance angle ϕ_s during this phase. YORP torques are not included in this simulation.

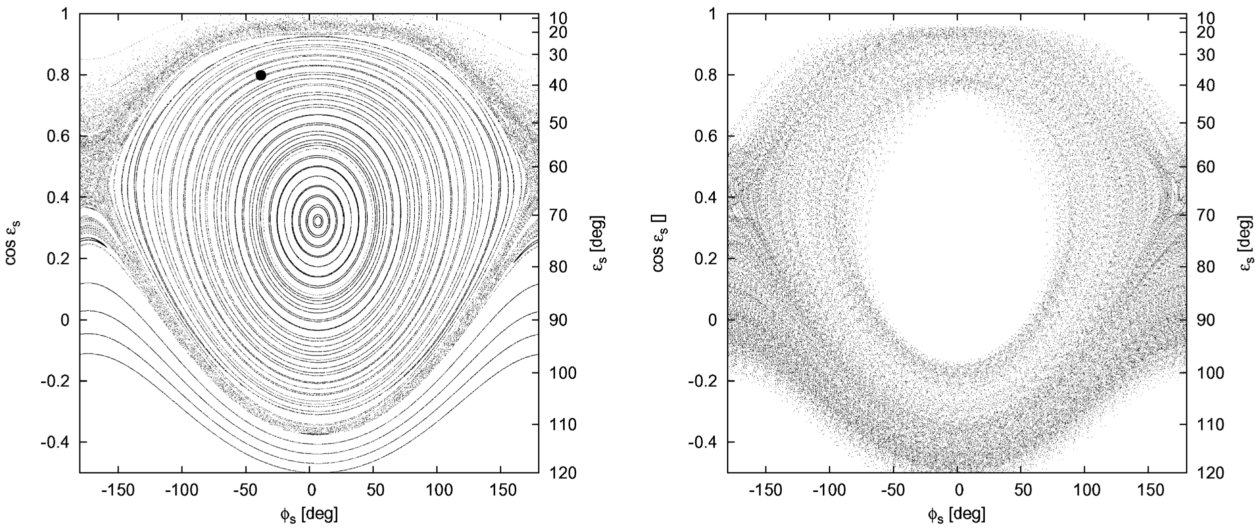

Fig. 19. Left: Surface-of-section for a toy model consisting of only two spectral lines in the Artemis' orbit non-singular inclination vector $\sin I/2\exp(\imath\Omega)$—proper s and the forced s_6. Amplitudes and phases taken from numerical analysis of the Artemis' orbit. Right: Artemis' spin integration over 50 My time interval (dots) projected onto the plane of resonant variables of the s secular spin–orbit resonance. Stability of the Cassini state 2 is clearly reduced in the complete model as a result of perturbations due to additional spectral lines in $\sin I/2\exp(\imath\Omega)$.

crowded with many more terms. Indeed, instead of finding stable librations about the Cassini state 2 of the s resonance, the spin often drops in and out of this resonance during our simulation. A significant reduction of the space of quasi-regular librations is also clearly seen in Fig. 19.

4. Examples of how spin dynamics in the inner-belt is affected by YORP torques

The previous analysis shows that long-term spin dynamics of prograde-rotating asteroids in the inner and central main belt is complicated by spin–orbit resonances. The full picture, however, is even more complicated for $D \lesssim 40$ km objects that are affected by the thermal (YORP) torques (e.g., Rubincam, 2000; Vokrouhlický and Čapek, 2002; Čapek and Vokrouhlický, 2004). As a zero-order approximation, we can simulate YORP torques as a slow change of the previously constant parameter $\xi = \Delta P_6$. This makes asteroid spin histories, described for the nominal set of parameters above, pass through an additional dimension of the changing parameter ξ. The spin dynamics here, though, is closely linked to the obliquity history; this means a complicated relationship exists between the previously-studied long-term cases and the very-long-term cases that are governed by changes in ξ. This section is "yet another initial step" in our effort to fully understanding these processes (see also Vokrouhlický and Čapek, 2002; Rubincam et al., 2002).

4.1. (951) Gaspra with YORP included

Gaspra's rotation state and its relation to the YORP effect is of interest for several reasons. First, it is the smallest asteroid in our sample; this means that the YORP effect can more readily modify its spin state than those of the other bodies discussed here. Rubincam (2000), using a model where the surface thermal conductivity (K) of Gaspra was set to zero, determined that a characteristic timescale to double Gaspra's rotation rate by YORP could be as short as 200–250 My. This value is comparable to or shorter than the age of the Flora family (Nesvorný et al., 2002). In a subsequent paper, Rubincam et al. (2002) pointed out that Gaspra's spin pole is residing close to the s resonance, which suggested to them that the previous YORP evolution may have drove the asteroid to this state. Although we cannot exclude this possibility, we argue below that this connection is less likely than the case of Slivan-state asteroids in the Koronis-family (Vokrouhlický et al., 2003).

Using the same shape model as described in Section 3.1, we confirm the results of Rubincam (2000), namely that for a Gaspra model with $K = 0$ W/m/K, YORP torques tend to tilt Gaspra's spin axis toward its orbital plane and decelerate its rotation rate. If K values are non-zero, however, these results are turned on their head. High K values ($\gtrsim$0.01 W/m/K) force the spin axis to evolve to an orientation perpendicular to the orbital plane, with its rotation rate accelerated (see also the evolution of (433) Eros; Čapek and Vokrouhlický, 2004). Interestingly, when K corresponds to a likely value for Gaspra ($\sim$0.005 W/m/K), YORP mainly affects the rotation rate; the obliquity experiences no meaningful changes (cf. Fig. 4 of Čapek and Vokrouhlický, 2004). Note that YORP-induced changes to the spin rate are weakly dependent of the K value. Thus, as a simplifying approximation in the work described below, we only account for how YORP secularly affects an asteroid's rotation rate and purposely neglect how it affects obliquity.

We start with the 50 My simulation of Gaspra's spin history as in Section 3.1 but now include our best estimate of the YORP torques (i.e., corresponding to Čapek and Vokrouhlický (2004) model with $K = 0.005$ W/m/K). We find that the result is essentially the same as that shown in Fig. 6; the spin state stays bound in the chaotic zone of the s resonance. There appears to be a minor modification of P from the initial value of 7.04 to 6.8 h at the end of our simulation, less then expected from the pure YORP model. This is because the switch from YORP-driven spin deceleration vs. acceleration occurs at $\sim$53° (see Rubincam, 2000; Fig. 4) and resonance effects make the obliquity oscillate about this value. As a result, there is no coherent accumulation of the YORP effect on the rotation rate of Gaspra. Only the slight asymmetry of obliquity oscillations near $\sim$53° force the rotation rate to slowly decrease. Over longer timescales, which are not studied here, this slow evolution may accelerate by bringing the s resonance toward the range of smaller obliquities (see Fig. 4).

We next considered possible past evolutionary paths for Gaspra's spin. In accordance with its cratering record and the dynamical evolution of the Flora family, we assume Gaspra is $\sim$(200–500) My. These timescales are computationally expensive to deal with in our spin vector evolution code. For this reason, we tracked the evolution of smaller asteroids and then scaled the results to the size of the asteroid in question (i.e., the strength of the YORP torques and hence the timescale needed to produce modifications to an asteroid's spin state are $\propto D^{-2}$, e.g., Rubincam, 2000). Thus, instead of considering the spin history of Gaspra with $D \sim 12$ km, we instead computed what happens to a $D = 3.64$ km size asteroid (a "pseudo-Gaspra," using the terminology of Rubincam, 2000) over a timescale of few tens of My. The chosen size ratio of the pseudo-Gaspra and real Gaspra is such that Gaspra's evolution would be a factor 10 longer than for pseudo-Gaspra. Thus the 50 My spin evolution of the latter translates into 500 My evolution of the former.[5]

We ran a series of simulations using small pseudo-Gaspra asteroids started with initial P values of 6, 7, 8, 8.5, 9 and 10 h. Their initial obliquities were chosen between 10°–80° with an increment of 10°. The initial longitude of the pseudo-Gaspra spin axis was that of Gaspra today, but this value had little influence on our conclusions. In total, we computed 48 simulations, each spanning 50 My.

---

[5] Note, our approach is not an exact scaling procedure of the dynamical Eq. (1) because it ignores the effects of gravitational and inertial torques on their right-hand sides. Nevertheless, it is a good zero-order approximation when the characteristic YORP timescale is still very long compared to any periodic effects resulting from the gravitational and inertial torques (such as the libration period about the Cassini state).

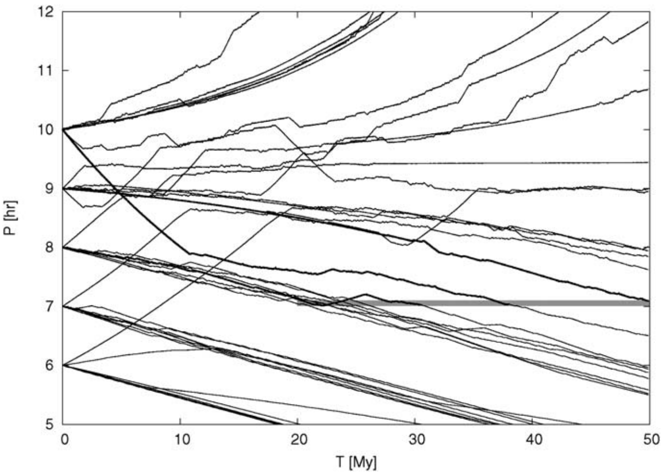

Fig. 20. Rotation period P (in h) from numerical simulations of pseudo-Gaspra starting with 5 different initial values (6, 7, 8, 9 and 10 h). Each time 8 different initial obliquity values in between 10° and 80° (with a step of 10°) is considered, thus altogether 40 evolutionary tracks are seen here. Only some of them manage to meet the currently observed rotation period of $\simeq$7.04 h shown in the shaded strip (its extension reflects uncertainty in the Gaspra's age, $\sim$(20–50) My in the timescale of our pseudo-Gaspra evolution). Three possible evolutionary tracks, with different initial rotation periods and obliquity values, are highlighted in bold.

Fig. 20 shows 40 evolutionary P tracks from our simulations. Interactions with secular spin–orbit resonances causes P to fluctuate; in fact in some cases the rate of change in P even temporarily changes its sign. Only some end up matching the pseudo-Gaspra spin-state constraints for the scaled age of $\sim$(20–50) My. The positive matches are for those whose initial P was larger than the current value, most likely in the range (7–10) h. Bold curves emphasize three such solutions that started with three different initial P values.

The evolution of Gaspra's obliquity for these 3 solutions is shown in Fig. 21. The diversity of results indicates that Gaspra's could have had a wide range of obliquity values in the past. Except for a short period of time, the solution in the upper panel is always confined to the chaotic zone located near the s resonance. The solution in the middle panel starts as a quasi-stable librator about the Cassini state 2 of the s resonance, but then it evolves out of this resonance. As P decreases, the resonance, together with its chaotic layer, increases in size. The bottom panel solution starts as regular circulation outside the s resonance, but as P decreases due to the YORP torques, it falls into its chaotic zone; this latter evolutionary tracks is perhaps the closest to the scenario envisaged by Rubincam et al. (2002).

We conclude from this that Gaspra's current rotation state is chaotic enough that an infinite number of past evolutionary tracks are possible. Except for some broad constraints, such as the likely value of Gaspra's initial P value, no definitive answer to the Gaspra's previous spin vector evolution can be given at this time.

Worse still is the fact that the anomalously large s resonance covers $\sim$30% of all prograde rotation states for Gaspra's current rotation period (see Fig. 4 and Henrard and Murigande, 1987). This means that a Gaspra spin state located near the outskirts of a chaotic zone does not necessarily mean it emerged from the resonance earlier in its history via YORP torques. We find a no-YORP model would still be statistically meaningful because a broad range of initial conditions could lead toward the current state. As such, the only true and a clear-cut case for past YORP evolution known to date are the group of prograde-rotating asteroids in the Koronis family (Slivan, 2002; Vokrouhlický et al., 2003).

4.2. (60) Echo and (32) Pomona with YORP included

The remaining test cases described in paper do not have precise shape models, which makes it difficult to accurately evaluate how YORP torques have affected their spin vectors. For this reason, we apply here statistical results from Čapek and Vokrouhlický (2004), who computed YORP torques for a large number of irregularly-shaped bodies. We use an average of their results, corresponding to the low thermal conductivity $K = 0.001$ W/m/K, as a characteristic YORP torque in our simulations.

A second issue is that the asteroids discussed below are significantly larger than Gaspra, such that YORP is less likely to have played a significant role in their past evolution. We can still use these bodies, however, as proxies of how YORP-related effects could modify the spin states of smaller asteroids with similar orbits. To do this, we scaled all of our results by a given factor. For example, our pseudo-Echo asteroid ($D = 3$ km) is a factor 20 smaller than Echo itself ($D = 60$ km). Thus, the timescale in our simulation should be scaled by a factor of 400 to infer how Echo may have evolved in the past.

The purpose of our simulation is to determine the importance of various dynamical structures that could complicate how spin vectors of small, inner main-belt asteroids have evolved with time. Fig. 22 shows an example run where we numerical tracked a pseudo-Echo that started with an initial obliquity of 70° and $P = 10$ h. We see that it has a fairly complex evolution: (i) it evolves through a non-resonant phase (0–7 My), (ii) it falls into the s resonance (7–20 My), (iii) it escapes the s resonance only to be captured into the weak secular resonance associated with the third spectral line in Fourier decomposition of $\sin I/2 \exp(\imath\Omega)$ at[6] $s_x \simeq -58$ arcsec/yr (20–33 My), and (iv) it evolves toward the slow-spinning YORP end-state seen in this figure (33–41 My). Its passage through the s resonance actually has two phases: (i) temporary librations about Cassini state 2 associated with large variations in obliquity, and (ii) oscillations about Cassini state 1 with much more confined obliquity variations. The secular trends while in the s and s_x resonances are driven by YORP deceleration of P for obliquity $\lesssim$54°. For example, between 20–33 My, the solution follows the motion of Cassini state 2 of the s_x resonance in the small libration regime. A similar situation was reported by Vokrouhlický et al. (2003) for the Koronis asteroids where the s_6 resonance played a similar role.

As an aside, we note that just as the asteroid is about to jump out of the s_x resonance, the spin state resembles that of (60)

---

[6] For sake of brevity we use s_x to denote frequency of this term since we were not able to properly track its origin.

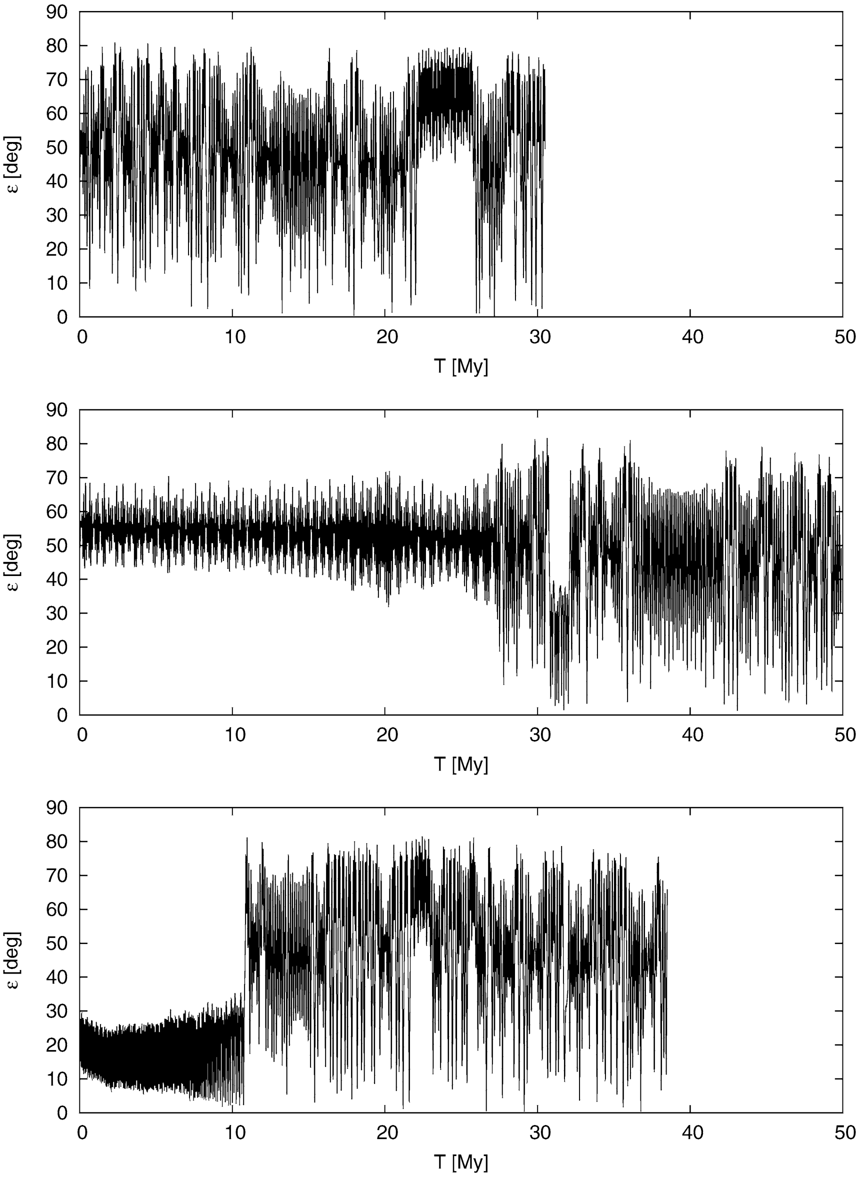

Fig. 21. Time-evolution of the osculating obliquity from numerical simulations of pseudo-Gaspra for the three highlighted tracks in Fig. 20. Upper panel starts with rotation period of 8 h and obliquity 40°, middle panel starts with rotation period of 9 h and obliquity 50°, and bottom panel starts with rotation period of 10 h and obliquity 20°; each of the cases meet parameters of the observed rotation state of Gaspra at their respective terminal times.

Echo. Thus, by scaling the results up to Echo's true size, the shaded interval in Fig. 22 potentially represents the evolution of Echo's spin state over the past 4 Gy. YORP perturbations would then be responsible for a $\sim 20°$ increase in the obliquity and an ~ 8 h increase of the rotation period, with the underlying transfer route being the s_x resonance (recall Echo is a $D = 60$ km size asteroid). There is obviously a large number of other possible evolutionary outcomes, but this one does a good job of illustrating the complexity one should expect in the spin vector histories of small bodies in the Solar System.

The steady increase in obliquity seen in Fig. 22, associated with small-amplitude resonant librations, might also be driven by the s resonance. In Section 3.3, we stated that Pomona's current rotation-state parameters do not support the existence of the s resonance. According to our simulation, however, when $P \sim 12$ h from YORP torques, the resonance bifurcates and immediately captures the pseudo-Pomona spin vector (Fig. 23). Further deceleration of the rotation rate makes the Cassini state migrate toward higher obliquity values, dragging the pseudo-Pomona spin state along at small-amplitude librations. Eventually, though, the amplitude increases to the point that the spin state reaches a chaotic zone near the resonance separatrix and leaves the resonance. Then, the spin state evolves toward the end state of the YORP cycle where the obliquity approaches zero. Compared to non-resonant case, the evolutionary track toward the YORP end state was significantly extended by capture into the resonance.

4.3. (105) Artemis with YORP included

In Sections 3.4 and 3.5, we stated that the spin histories of objects residing on high-inclination orbits are strongly affected

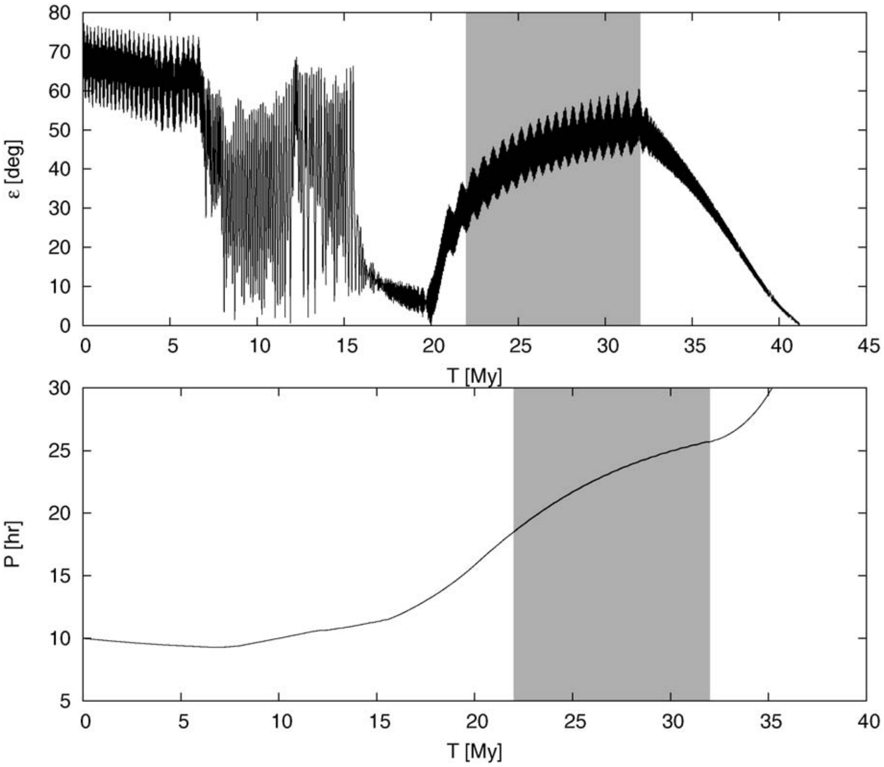

Fig. 22. A toy model for a possible past evolution of 60 Echo spin state. Osculating obliquity ϵ (top) and rotation period P (bottom) as a function of time for a 3 km size object on the current Echo's orbit. For a 60 km body the timescale would stretch by a factor $\sim 20^2 = 400$, thus the shaded segment might correspond to ∼4 Gy time interval for that body.

by the large size of the s resonance. In this section, we investigate its further implications within our spin vector evolution model that includes YORP torques.

As before, we propagated the spin histories of pseudo-Artemis test asteroids ($D = 3$ km) residing in the same orbit as the real Artemis. To obtain a better statistical characterization of our results, we ran 21 close clones[7] starting from Artemis' current spin state and then tracked them 50 My into the future. For each case, we allowed the rotation rate to both accelerate and decelerate (see Čapek and Vokrouhlický, 2004) via averaged YORP torques. Thus in total, we performed 42 simulations.

Fig. 24 shows 3 characteristic evolutionary tracks of pseudo-Artemis obliquity. The upper panel shows a case where, for the entire evolutionary span, the spin axis either librated about Cassini state 2 of the s resonance or adhered to its separatrix. The ϵ value in the middle panel eventually decelerated enough that the spin axis dropped out of the s resonance permanently; this allowed it to evolve toward the YORP endstate of zero obliquity without entering another resonance. Interestingly, there were 13 cases among our 42 simulations that were similar to the evolution shown in the bottom panel. Like the previous cases, ϵ left the s resonance but this time it reached far enough into the retrograde-rotating state (obliquity $\geqslant 90°$) that it ultimately evolved toward the YORP end state of 180° obliquity. In this manner, the initially prograde-rotating states can feed the retrograde-rotating states in course of the YORP evolution. Note that the reverse process, with the retrograde states evolving toward the prograde ones, is unlikely because there are no significant secular spin–orbit resonances affecting retrograde rotation. The strongest of them, with frequency $\simeq +77$ arcsec/yr and forced amplitude of $\simeq 0.5°$ in $\sin I/2 \exp(\imath \Omega)$, affects the evolution at ∼150° obliquity. This trend toward retrograde rotation states implies that asteroids residing on high inclination orbits, such as the Phocaeas and Hungarias, may have obliquity values that are somewhat skewed toward retrograde rotation states. This hypothesis might be tested by observing Hungaria asteroids, which happen to be the closest high inclination population to Earth on stable orbits.

5. Discussion and conclusions

Our runs indicate that the long-term evolution of asteroid spin vectors can be extremely chaotic and complex for inner main-belt asteroids. The main reason for this is that they are strongly affected by interacting spin–orbit resonances. The issue in front of us now is whether this information can be used to determine the statistical parameters of a large sample of asteroids. Note that this problem was previously addressed by Skoglöv (1999) and Skoglöv and Erikson (2002), who predicted that asteroids should have a fairly uniform obliquity distribution but that a small excess of asteroids with large obliquities was possible. Their results were based on an analysis of a limited number of test asteroids whose spin states were tracked for short integration timescales.

---

[7] These clones were produced by adding ±0.01° to the nominal value of the pole longitude for Artemis; other spin parameters were kept the same.

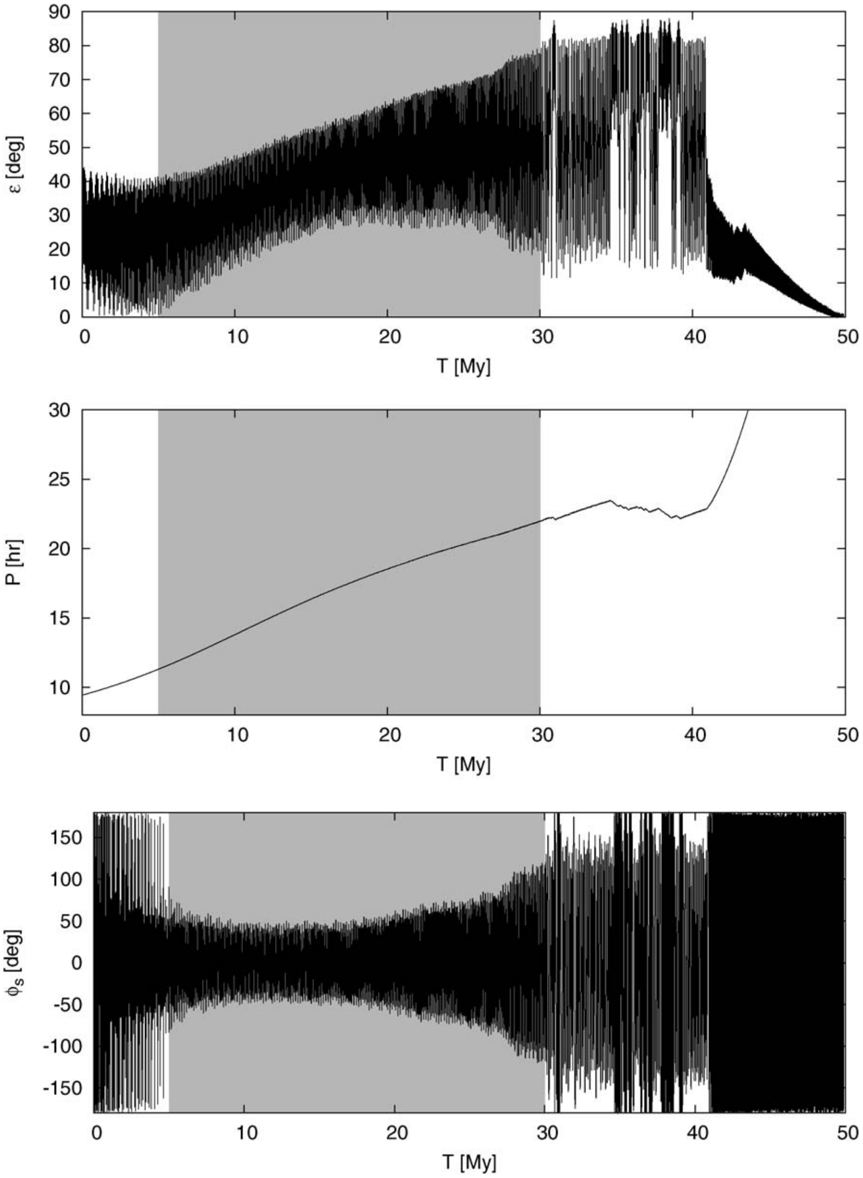

Fig. 23. Spin-state evolution for pseudo-Pomona asteroid (size 3 km) and YORP torques included. Initial data that of the currently observed spin state of (32) Pomona. Upper panel is the osculating obliquity, middle panel is the rotation period P and bottom panel is the resonant angle ϕ_s of the s resonance. During the time interval pointed out by the dashed interval the spin axis librates about the Cassini state 2 of the s resonance. After leaving the chaotic buffer near separatrix of this resonance, the evolution heads toward the zero-obliquity end-state of the YORP evolution.

Here we repeat their experiment, but in our case we have brought both our model and additional computational power to bear on the problem. Our method was to numerically track the spin vector evolution of pseudo-Gaspras over a range of initial parameters. We assumed a fixed initial rotation period of $P = 7.04$ h (YORP was not included at this stage of analysis) and a grid of 40 equidistant values of $\cos \epsilon_s$ and 36 values of ϕ_s (recall ϵ_s and ϕ_s are obliquity and resonant angles in the reference frame of s resonance). Thus, in total we performed 1440 numerical simulations, each spanning 2 My (sufficiently longer than any period seen in the obliquity oscillations). At each timestep, i.e., each 200 yr, we recorded the position of the spin axis in the same grid that defined the initial data. This procedure allowed us to compute the time spent by each spin axis over a series of cells in ϵ_s and ϕ_s.

By folding together all ϕ_s values, we obtained a distribution in Fig. 25 that corresponds to an expected equilibrium distribution of obliquity values. Our results indicate the resultant obliquity distribution is fairly uniform. No clustering was observed in the longitude angle ϕ_s. Each initial latitude bin among the prograde rotators was nearly-equally populated by all prograde states, while each of the initially retrograde latitude bins was populated mostly the same and neighboring bins. We repeated our numerical experiment for different values of initial P, namely 5.3, 10.5 and 21 h. All results closely resembled that in Fig. 25, with slightly larger fluctuations for longer rotation periods. Thus, in the end, we arrived at a similar conclusion to that of Skoglöv (1999) and Skoglöv and Erikson (2002). The chaos that affects prograde rotators, together with a quasi-regularity among retrograde rotators, produces a uniform

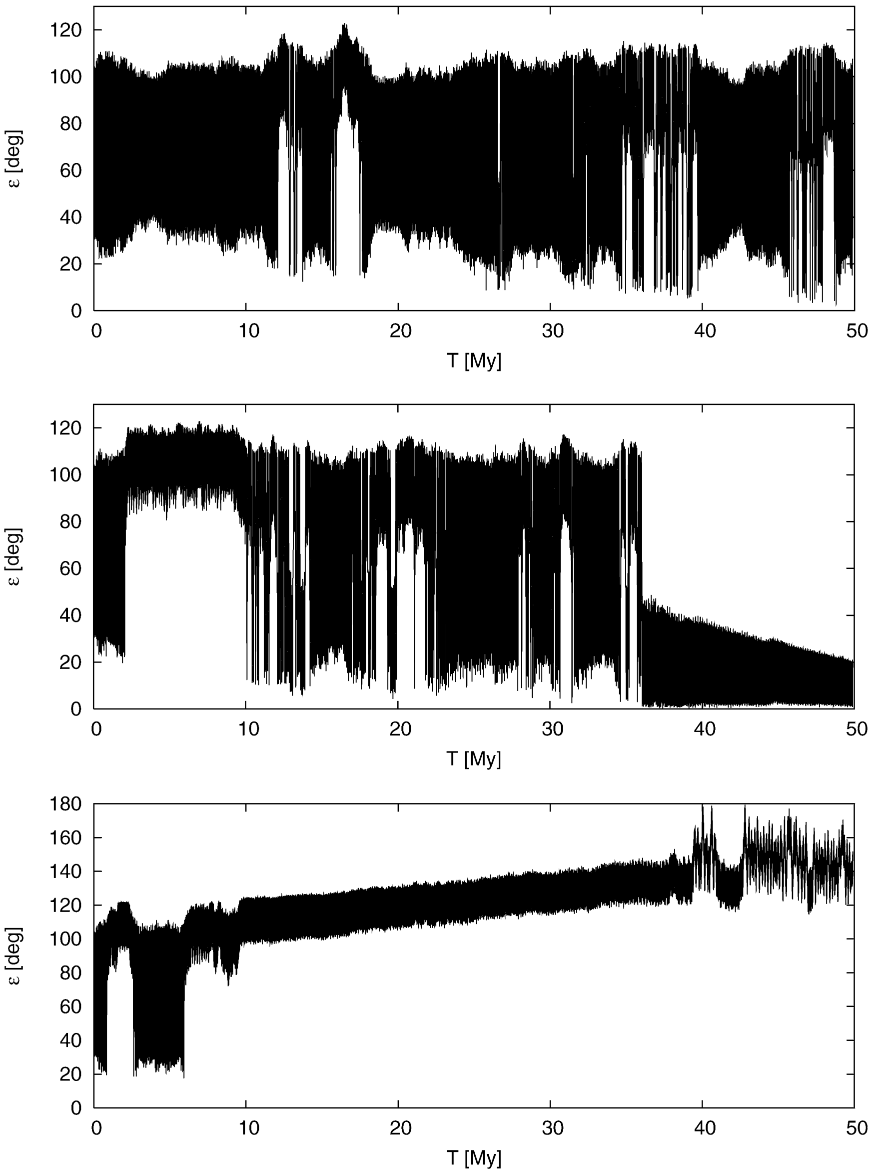

Fig. 24. Three characteristic evolution scenarios for obliquity in our simulations of pseudo-Artemis (size 5 km) and YORP torques included. The upper panel shows the spin state permanently confined, or adhered, to the s resonance. The bottom two panels are examples of tracks that left the s resonance and evolved toward the end-states of YORP cycle: either 0° obliquity (middle) or 180° obliquity (bottom). For high-inclination orbits this feeding of retrograde spin state from initially prograde ones is a significant phenomenon and may affect distribution of obliquities among Phocaea and/or Hungaria populations.

obliquity distribution (provided the initial data were also uniform). Because our data does not include YORP torques, we consider these results applicable to $D > 50$ km asteroids.

Skoglöv and Erikson (2002) pointed out that asteroids on low- and high-inclinations orbits may have different latitude distributions for their rotation poles. This evidence at present is based purely on observational work; no dynamical mechanism has yet been identified that can explain this difference. For this reason, we repeated our numerical experiment by determining what happens to an object on the high-inclination orbit of Artemis with rotation periods of $P = 12$ and 18 h. By tracking the time spent by the rotation vector at various latitudes, we determined the expected equilibrium distribution of the ecliptic latitude (Fig. 26). We find that it appears to be fairly uniform, except possibly the first bin for $P = 18$ h. It is possible, however, that the integration timescale was a factor in our results; future work will be used to confirm this.

We thus conclude that large asteroids have not had their obliquity values and ecliptic latitudes significantly affected by long-term chaotic dynamics. This implies that the bimodality of obliquities observed among large asteroids, which are skewed toward the ecliptic poles, may be primordial (i.e., were produced during the planetesimal formation epoch; Pravec et al., 2002; Bottke et al., 2005). To confirm this, a detailed study of the spatial distribution of the spin axes needs to be coupled with an analysis of their rotation frequency distribution. This work must also account for various factors such as orbital location in the main belt, asteroid size, observational selection effects, the effects of YORP on small bodies, etc. We consider this task beyond the scope of the present paper, but we

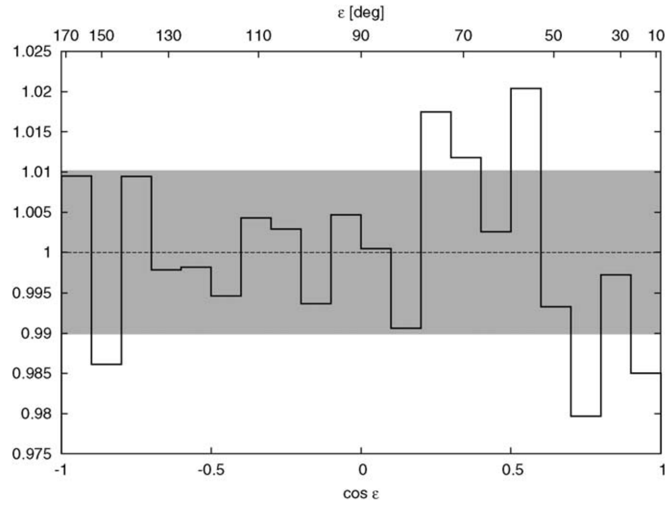

Fig. 25. Distribution of equilibrium $\cos\epsilon_s$ from our numerical experiment where numerous spin histories were started on a uniform grid of $(\cos\epsilon_s, \phi_s)$ values. Orbital and physical parameters were that of (951) Gaspra, including the rotation period 7.04 h. Occupancy in each bin is normalized to an average expected value, thus unity would mean a uniform distribution. We see small fluctuations about this value that only occasionally exceed one sigma level from Poissonian statistics (shown as a shaded interval; note the ordinate shows only a small interval of values near unity). This may be due to insufficient length of the integration (2 My).

believe the analytical and numerical methods described here will allow us to realistically attack this problem in the near future.

Next, we address how secular spin dynamics affect our efforts to model the dynamical evolution of various asteroid families via the Yarkovsky effect. Vokrouhlický et al. (2006a, 2006b, 2006c) found that many asteroid families have unusual semimajor axis distributions, with many smaller family members concentrated skewed toward extreme values. They interpreted these features as being the byproduct of a combination of thermal effects: (i) YORP torques driving the spin poles of small family members toward orientations that are normal to the ecliptic, and (ii) changes in the spin vector direction producing an increase in their Yarkovsky $\mathrm{d}a/\mathrm{d}t$ drift rates. By modeling these coupled effects and then comparing their results to observations, Vokrouhlický et al. (2006a, 2006b, 2006c) showed they could use the semimajor axis distribution of asteroid families to determine a family's approximate age of formation.

Vokrouhlický et al., however, did not consider how the evolution of asteroid spin axis orientations were affected by overlapping spin–orbit resonances. We briefly examine this issue here by tracking how gravitational and YORP torques affect the spin evolution of a $D = 3$ km body with the orbit and shape of (951) Gaspra. Here we use the mean thermal torque values derived by Čapek and Vokrouhlický (2004) for such a body. We assume the thermal conductivity is $K = 0.001$ W/m/K, while the specific heat capacity was set to $C_p = 680$ J/kg/K and bulk/surface densities were 2.5 g/cm^3. Our analysis considered the possibility that the body's rotation rate might accelerate or decelerate via YORP torques. The spin integration timespan was limited to 50 My, the length of our orbital integration. We started our test asteroid with different values of the initial obliquity ϵ_0 and precession longitude $\psi_0 = 0°$, with the latter not affecting our results. In each case, we determined the total accumulated semimajor axis change $\Delta a = \int \mathrm{d}a$. Note that we used the linearized thermal theory to estimate $\mathrm{d}a = (\mathrm{d}a/\mathrm{d}t)_{\mathrm{Yarkovsky}}\mathrm{d}t$ and the obliquity- and spin-rate-dependent value of the Yarkovsky semimajor axis drift $(\mathrm{d}a/\mathrm{d}t)_{\mathrm{Yarkovsky}}$ (e.g., Vokrouhlický, 1999). For sake of comparison, we also computed the accumulated semimajor axis change when only the YORP torques were activated (and the effect of gravitational and inertial torques neglected); this was the same approximation used by Vokrouhlický et al. (2006a, 2006b, 2006c).

Fig. 27 summarizes our results. Retrograde rotators ($\cos\epsilon_0 < 0$) are unaffected by gravitational torques and the YORP-only model does a good job of estimating their accumulated semimajor axis change over time. As expected, we found the body

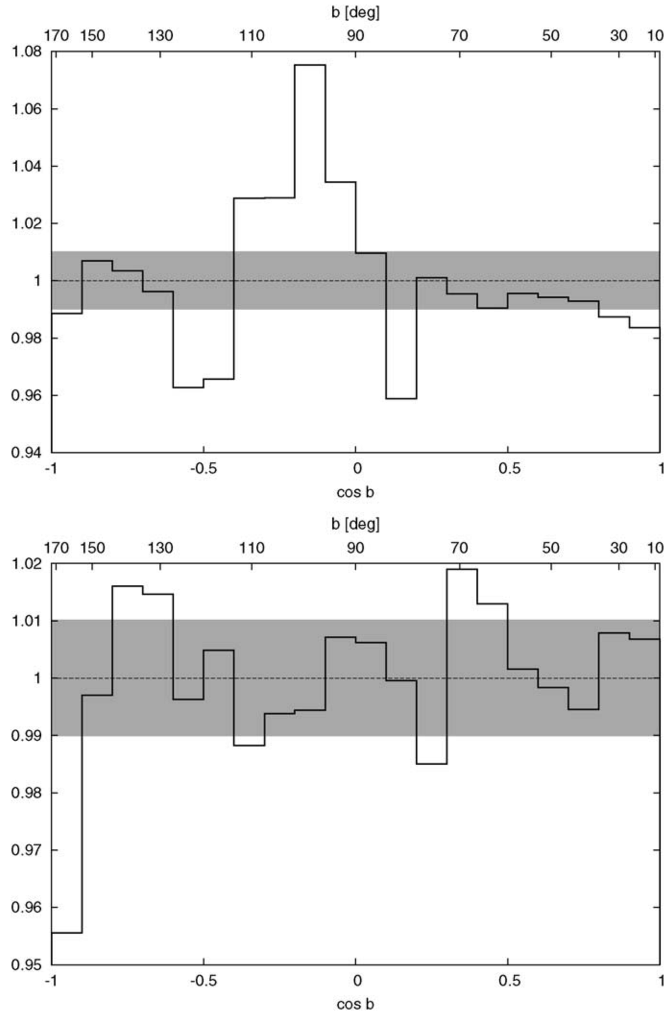

Fig. 26. Distribution of equilibrium $\cos b$ (b is the ecliptic latitude) from our numerical experiment where numerous spin histories were started on a uniform grid of $(\cos\epsilon_s, \phi_s)$ values. Orbital and physical parameters were that of (105) Artemis. The upper panel is for the rotation period 12 h, the lower for 18 h (close to Artemis' real value). Occupancy in each bin is normalized to an average expected value, thus unity would mean a uniform distribution. We see small fluctuations about this value that only occasionally exceed one sigma level from Poissonian statistics (shown as a shaded interval; note the ordinate shows only a small interval of values near unity). This may be due to insufficient length of the integration (2 My).

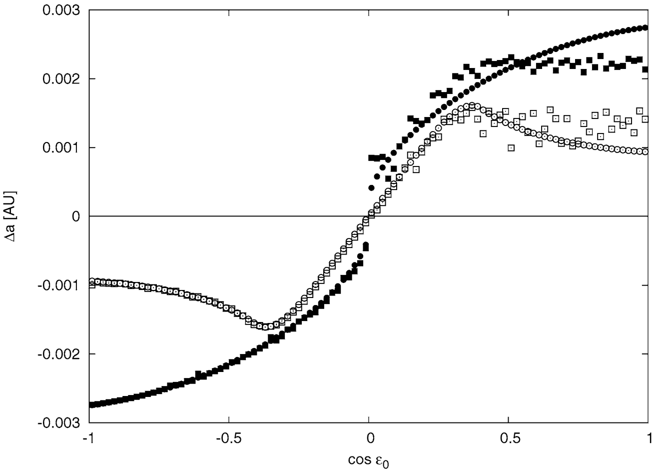

Fig. 27. For each initial obliquity ϵ_0 at the abscissa we determined the accumulated change of the semimajor axis Δa due to the Yarkovsky forces in 50 My. Pseudo-Gaspras with $D = 3$ km were assumed and the surface thermal conductivity was set to 0.001 W/m/K, specific heat capacity to 680 J/kg/K and surface/bulk density to 2.5 g/cm^3. Open/full symbols were determined for average YORP torques that asymptotically decelerate/accelerate asteroid's rotation. Model where we included only the YORP torques is shown with circles; model that additionally contains the effects of gravitational torques is shown with squares. The YORP-only results are characterized by: (i) decrease of $|\Delta a|$ for extreme initial values of ϵ_0 in the case when the rotation period becomes very long by YORP (because the thermal lag angle producing the orbital effect rapidly shrinks), (ii) relative decrease of $|\Delta a|$ for extreme initial values of ϵ_0 in the case when the rotation period becomes short by YORP (because the dominant diurnal variant of the Yarkovsky effect ceases to be efficient for fast rotation). Secular spin–orbit resonances (s and s_6) produce Δa fluctuating about a mean value for initially prograde rotators in the model where the gravitational torques have been included. While the difference is not very large, our results may imply the asteroid families' ages may have been slightly underestimated in Vokrouhlický et al. (2006a, 2006b, 2006c).

drifted $\sim 10^{-3}$ AU in 50 My. This is because gravitational torques for retrograde rotators produce uniform precession with constant obliquity. For prograde rotators, the YORP-only model produces the same accumulated Δa as retrograde rotators (with a changed sign).

When gravitational torques were included in the simulation, however, the presence of spin–orbit secular resonances s and s_6 had a strong effect on the accumulated Δa. We found a "flattenting" of Δa for $\cos\epsilon_0 \geqslant 0.3$ (and over a timespan of 50 My), mainly because gravitational torques are driving large obliquity ϵ changes. For individual objects, this means their Yarkovsky drift rates may increase for a time before decreasing (or vice versa). In certain cases, they may even change their sign multiple times. Chaotic mixing of the obliquity histories make the result nearly independent of ϵ_0. The net effect after 50 My is that Δa increases for the YORP-decelerating spins and decreases for YORP-accelerating spins. Between these two effects, the decelerating spin case is perhaps less important because bodies achieving long rotation periods are susceptible to be reoriented and spun up by non-disruptive collisions. We argue that the accelerating rotation rate case are more significant and hence may imply that families spread more slowly in a than predicted by our models. Consequently, some of the family ages derived by Vokrouhlický et al. (2006a, 2006b, 2006c) using the Yarkovsky/YORP effects alone may be shorter than the true ages. A detailed analysis of this effect for particular asteroid families will be the study of the next paper in this series.

Acknowledgments

The work of D.V. has been partly supported by the Grant Agency of the Czech Republic (Grant 205/05/2737); work by D.N. and W.F.B. was supported by NASA's Planetary Geology & Geophysics program and Discovery Data Analysis programs. We thank David Čapek for help in computing the YORP torques on (951) Gaspra and David P. Rubincam for suggestions on the first version of the paper.

Appendix A. A simple resonance-overlap criterion

Here we show a simple variant of the secular spin–orbit resonance overlap criterion that is based on our analysis of the Hamiltonian (7). We first note that in a single-line representation of the orbital-plane motion in space ($I = \text{const.}$ and $\Omega = st + \varphi$), a canonical transformation brings (7) into a form

$$\mathcal{H}_{\text{res}} = \frac{\alpha}{2}\left(X - \frac{s\cos I}{\alpha}\right)^2 + s\sqrt{1 - X^2}\sin I\cos\phi, \tag{A.1}$$

with $X = -\cos\epsilon$ and $\phi = -(\psi + \Omega)$. We assume here 4 equilibria exist for a given set of parameters. We are mainly concerned about Cassini states 2 and 4 that are the stable and unstable loci of the spin–orbit resonance. Though the algebra can be worked out in an implicit manner and easily programmed on a computer, our goal here is to provide a simplified, but analytic, form of the criterion for secular resonance to overlap (and thus likely trigger a chaotic boundary near their separatrixes; e.g., Chirikov, 1979; Wisdom, 1987). For that reason, we approximate the stable point location with $X_{\text{res}} \sim s\cos I/\alpha$. Using perturbation calculations in the immediate vicinity of the resonance location X_{res}, we approximate the resonance Hamiltonian (A.1) with a pendulum. The resonance width then reads

$$W \simeq 2\sqrt{\frac{|s|\sin I}{\alpha}}\left(1 - \frac{s^2\cos^2 I}{\alpha^2}\right)^{1/4}. \tag{A.2}$$

Now we can assume that two different frequencies s_1 and s_2 contribute to the motion of the orbital plane. We formally associate resonance zones with each of them and consider an approximate criterion for their overlap. Note this is not done using a full analysis of the 4-D phase space of the problem. Rather, we simply compare the maximum obliquity range covered by each of the resonances and determine whether it has a non-zero overlap. This occurs when

$$|s_1\cos I_1 - s_2\cos I_2| \lesssim \alpha(W_1 + W_2), \tag{A.3}$$

or if both inclinations I_1 and I_2 are small we may even write

$$|s_1 - s_2| \lesssim 2\sqrt{\alpha}\left(\sqrt{|s_1|\sin I_1} + \sqrt{|s_2|\sin I_2}\right). \tag{A.4}$$

Recall $\alpha \simeq 1330.6\xi/a^3$ arcsec/yr, where the semimajor axis a is given in AU and $\xi = \Delta P_6$, with P_6 the rotation period in 6 h increments. One of the two frequencies (s_2, say) is constant

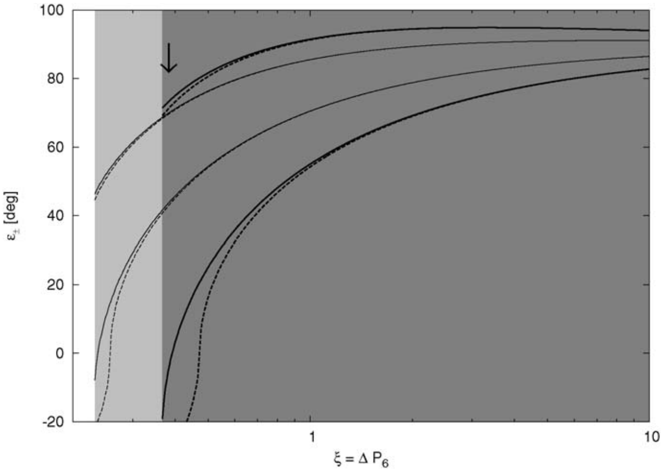

Fig. 28. Minimum ϵ_- and maximum ϵ_+ obliquity values of the secular spin–orbit resonance associated with the s (thick lines) and s_6 (thin lines) Fourier modes in Gaspra's non-singular inclination vector $\sin I/2 \exp(\iota\Omega)$ as a function of the physical parameter $\xi = \Delta P_6$ (Δ is the dynamical flattenting and P_6 is rotation period in 6 h units). Solid lines are the exact solution of the Colombo top, while the dashed lines are the approximate (pendulum-like) solution from Appendix A. The s_6 resonance bifurcates first and exists for the ξ values in the light-shaded zone. The s resonance bifurcates next, and exists together with the s_6 resonance in the dark-shaded zone. Gaspra's value $\xi \simeq 0.358$ indicated by the arrow places this asteroid right at the place where the s resonance starts to exist. YORP evolution may increase or decrease ξ by changing the asteroid's rotation period. For larger ξ values both resonances shrink and migrate toward larger obliquity values, nevertheless they always remain overlapped.

throughout the whole belt and amounts to -26.34 arcsec/yr. The corresponding forced inclination is $I_2 \sim 1^\circ$. The first line is the proper mode (s, I) of the orbital plane precession in space. The smaller is the difference on the left-hand side of (A.4) as compared to the sum of the resonance widths on the right-hand side, the more important is the effect of the resonance overlap and the more chaotic (irregular) evolution of the spin axis in space is expected.

Fig. 28 shows how well this approximate formulation compares to the exact solution of the Colombo top for (951) Gaspra. Except for the parameter interval near the bifurcation of the resonance, this approximate analytic approach does a good job at estimating the width of the resonance (and hence can also be used to determine the resonance overlap criterion).

We also note that asteroid (8) Flora has a comparable orbit to (951) Gaspra. Because its obliquity value is also similar, Gaspra's long-term spin evolution (see Section 3.1) may be similar to Flora's. There are differences to consider, though. Flora is much larger than Gaspra, it has a smaller flattenting parameter ($\Delta \simeq 0.17$), and its rotation period $P = 12.80$ h is longer (e.g., Torppa et al., 2003). Interestingly, Gaspra and Flora still have about the same value of $\xi = \Delta P_6$ which is the essential parameter needed to determine the precession rate. Indeed, our numerical propagation of Flora's spin state for 50 My indicates its obliquity chaotically wanders over the same large interval as that of Gaspra.

References

Bertotti, B., Farinella, P., Vokrouhlický, D., 2003. Physics of the Solar System. Kluwer Academic, Dordrecht.

Bottke, W.F., Vokrouhlický, D., Rubincam, D.P., Brož, M., 2002a. Dynamical evolution of asteroids and meteoroids using the Yarkovsky effect. In: Bottke, W.F., Cellino, A., Paolicchi, P., Binzel, R.P. (Eds.), Asteroids III. Univ. of Arizona Press, Tucson, pp. 395–408.

Bottke, W.F., Morbidelli, A., Jedicke, R., Petit, J.M., Levison, H.F., Michel, P., Metcalfe, T.S., 2002b. Debiased orbital and magnitude distribution of the near-Earth objects. Icarus 156, 399–433.

Bottke, W.F., Durda, D.D., Nesvorný, D., Jedicke, R., Morbidelli, A., Vokrouhlický, D., Levison, H.F., 2005. Linking the collisional history of the main asteroid belt to its dynamical excitation and depletion. Icarus 179, 63–94.

Bowell, E., Muinonen, K., Wasserman, L.H., 1994. A public-domain asteroid orbit data base. In: Milani, A., di Martino, A., Cellino, A. (Eds.), Asteroids, Comets, Meteors 1993. Kluwer Academic, Dordrecht, pp. 477–481.

Breiter, S., Nesvorný, D., Vokrouhlický, D., 2005. Efficient Lie–Poisson integrator for secular spin dynamics of rigid bodies. Astron. J. 130, 1267–1277.

Čapek, D., Vokrouhlický, D., 2004. The YORP effect with finite thermal conductivity. Icarus 172, 526–536.

Chapman, C.R., 2002. Cratering on asteroids from Galileo and NEAR Shoemaker. In: Bottke, W.F., Cellino, A., Paolicchi, P., Binzel, R.P. (Eds.), Asteroids III. Univ. of Arizona Press, Tucson, pp. 315–330.

Chirikov, B.V., 1979. A universal instability of many dimensional oscillator systems. Phys. Rep. 52, 263–379.

Colombo, G., 1966. Cassini's second and third laws. Astron. J. 71, 891–896.

Correia, A.C.M., Laskar, J., 2001. The four final rotation states of Venus. Nature 411, 767–770.

Correia, A.C.M., Laskar, J., 2004. Mercury's capture into the 3/2 spin–orbit resonance as a result of its chaotic dynamics. Nature 429, 848–850.

Davies, M.E., Colvin, T.R., Belton, M.J.S., Veverka, J., Thomas, P.C., 1994. The direction of the North Pole and the control network of Asteroid 951 Gaspra. Icarus 107, 18–22.

Donnison, J.R., Wiper, M.P., 1999. Bayesian statistical analysis of asteroid rotation rates. Mon. Not. R. Astron. Soc. 302, 75–80.

Fulchignoni, M., Barucci, M.A., di Martino, M., Dotto, E., 1995. On the evolution of the asteroid spin. Astron. Astrophys. 299, 929–932.

Goldreich, P., Peale, S.J., 1968. The dynamics of planetary rotations. Annu. Rev. Astron. Astrophys. 6, 287–320.

Greenberg, R., Nolan, M.C., Bottke, W.F., Kolvoord, R.A., Veverka, J., 1994. Collisional history of Gaspra. Icarus 107, 84–97.

Hamilton, D.P., Ward, W.R., 2004. Tilting Saturn. I. Numerical model. Astron. J. 128, 2510–2517.

Henrard, J., Murigande, C., 1987. Colombo's top. Celest. Mech. 40, 345–366.

Holland, R.L., Sperling, H.J., 1969. A first-order theory for the rotational motion of a triaxial rigid body orbiting an oblate primary. Astron. J. 74, 490–496.

Kaasalainen, M., 2004. Physical models of large number of asteroids from calibrated photometry sparse in time. Astron. Astrophys. 422, L39–L42.

Kaasalainen, M., Torppa, J., Piironen, J., 2002. Models of twenty asteroids from photometric data. Icarus 159, 369–395.

La Spina, A., Paolicchi, P., Kryszczyńska, A., Pravec, P., 2004. Retrograde spins of near-Earth asteroids from the Yarkovsky effect. Nature 428, 400–401.

Laskar, J., Robutel, P., 1993. The chaotic obliquity of the planets. Nature 361, 608–612.

Levison, H., Duncan, M., 1994. The long-term dynamical behavior of short-period comets. Icarus 108, 18–36.

Lissauer, J.J., Dones, L., Ohtsuki, K., 2000. Origin and evolution of terrestrial planet rotation. In: Canup, R.M., Righter, K. (Eds.), Origin of the Earth and Moon. Univ. of Arizona Press, Tucson, pp. 101–112.

Michałowski, T., 1993. Poles, shapes, senses of rotation, and sidereal periods of asteroids. Icarus 106, 563–572.

Morbidelli, A., 2002. Modern Celestial Mechanics: Aspects of Solar System Dynamics. Taylor & Francis, London.

Morbidelli, A., Vokrouhlický, D., 2003. The Yarkovsky-driven origin of near Earth asteroids. Icarus 163, 120–134.

Nesvorný, D., Morbidelli, A., Vokrouhlický, D., Bottke, W.F., Brož, M., 2002. The Flora family: A case of the dynamically dispersed collisional swarm? Icarus 157, 155–172.

Néron de Surgy, O., Laskar, J., 1997. On the long term evolution of the spin of the Earth. Astron. Astrophys. 318, 975–989.

Pravec, P., Harris, A.W., Michałowski, T., 2002. Asteroid rotations. In: Bottke, W.F., Cellino, A., Paolicchi, P., Binzel, R.P. (Eds.), Asteroids III. Univ. of Arizona Press, Tucson, pp. 113–122.

Pravec, P., and 19 colleagues, 2005. Tumbling asteroids. Icarus 173, 108–131.

Rubincam, D.P., 2000. Radiative spin-up and spin-down of small asteroids. Icarus 148, 2–11.

Rubincam, D.P., Rowlands, D.D., Ray, R.D., 2002. Is Asteroid 951 Gaspra in a resonant obliquity state with its spin increasing due to YORP? J. Geophys. Res. 107 (E9), 5065.

Skoglöv, E., 1997. Evolution of the obliquities for nine near-Earth asteroids. Planet. Space Sci. 45, 439–447.

Skoglöv, E., 1999. Spin vector evolution for inner Solar System asteroids. Planet. Space Sci. 47, 11–22.

Skoglöv, E., Erikson, A., 2002. The influence of the orbital evolution of main-belt asteroids on their spin vectors. Icarus 160, 24–31.

Skoglöv, E., Magnusson, P., Dahlgren, M., 1996. Evolution of the obliquities for ten asteroids. Planet. Space Sci. 44, 1177–1183.

Slivan, S.M., 2002. Spin vector alignment of Koronis family asteroids. Nature 419, 49–51.

Souchay, J., Bouquillon, S., 2005. The high frequency variations in the rotation of Eros. Astron. Astrophys. 433, 375–383.

Souchay, J., Kinoshita, H., Nakai, H., Roux, S., 2003. A precise modeling of Eros 433 rotation. Icarus 166, 285–296.

Tedesco, E.F., Noah, P.V., Noah, M., Price, S.D., 2002. The supplemental IRAS minor planet survey. Astron. J. 123, 1056–1085.

Thomas, P.C., Veverka, J., Simonelli, D., Helfenstein, P., Carcich, B., Belton, M.J.S., Davies, M.E., Chapman, C., 1994. The shape of Gaspra. Icarus 107, 23–36.

Torppa, J., Kaasalainen, M., Michałowski, T., Kwiatkowski, T., Kryszczyńska, A., Denchev, P., Kowalski, R., 2003. Shapes and rotational properties of thirty asteroids from photometric data. Icarus 164, 346–383.

Tungalag, N., Schevchenko, V.G., Lupishko, D.F., 2002. Rotation parameters and shapes of 15 asteroids. Kin. Phys. Celest. Bodies 18 (6), 508–516. In Russian.

Vokrouhlický, D., 1999. A complete linear model for the Yarkovsky thermal force on spherical asteroid fragments. Astron. Astrophys. 344, 362–366.

Vokrouhlický, D., Čapek, D., 2002. YORP-induced long-term evolution of the spin state of small asteroids and meteoroids: Rubincam's approximation. Icarus 159, 449–467.

Vokrouhlický, D., Nesvorný, D., Bottke, W.F., 2003. The vector alignments of asteroid spins by thermal torques. Nature 425, 147–152.

Vokrouhlický, D., Bottke, W.F., Nesvorný, D., 2005. The spin state of 433 Eros and its possible implications. Icarus 175, 419–434.

Vokrouhlický, D., Brož, M., Bottke, W.F., Nesvorný, D., Morbidelli, A., 2006a. Yarkovsky/YORP chronology of asteroid families. Icarus 182, 118–142.

Vokrouhlický, D., Brož, M., Morbidelli, A., Bottke, W.F., Nesvorný, D., Lazzaro, D., Rivkin, A.S., 2006b. Yarkovsky footprints in the Eos family. Icarus 182, 92–117.

Vokrouhlický, D., Brož, M., Bottke, W.F., Nesvorný, D., Morbidelli, A., 2006c. The peculiar case of the Agnia asteroid family. Icarus. In press.

Ward, W.R., Hamilton, D.P., 2004. Tilting Saturn. I. Analytic model. Astron. J. 128, 2501–2509.

Wisdom, J., 1987. Urey prize lecture: Chaotic dynamics in the Solar System. Icarus 72, 241–275.

Wisdom, J., 2004. Spin–orbit secondary resonance dynamics of Enceladus. Astron. J. 128, 484–491.

Wisdom, J., 2006. Dynamics of the lunar spin axis. Astron. J. 131, 1864–1871.

Wisdom, J., Peale, S.J., Mignard, F., 1984. The chaotic rotation of Hyperion. Icarus 58, 137–152.